The Dissertation Committee for Gail Ruth Muldoon
certifies that this is the approved version of the following dissertation:

West Antarctic Ice Sheet Retreat during the Last Interglacial

Committee:

Charles S. Jackson, Co-Supervisor

Donald D. Blankenship, Co-Supervisor

Omar Ghattas

Patrick Heimbach

Terrence M. Quinn

Duncan A. Young

West Antarctic Ice Sheet Retreat during the Last Interglacial

by

Gail Ruth Muldoon

DISSERTATION
Presented to the Faculty of the Graduate School of
The University of Texas at Austin
in Partial Fulfillment
of the Requirements
for the Degree of

DOCTOR OF PHILOSOPHY

THE UNIVERSITY OF TEXAS AT AUSTIN
May 2018

To my husband.

Acknowledgments

I'm grateful to my defense committee for their guidance and support conducting this research. I thank Charles Jackson for hiring me at the start of this journey and for 7 years of never wanting for a supercomputer allocation. I thank Don Blankenship for contributing his vision to this project and for encouraging the field component of this research. I thank Duncan Young for invaluable thoughtfulness, practical advice, and feedback without which this work may not have been completed. I also thank the other members of my committee, Drs. Terry Quinn, Omar Ghattas, and Patrick Heimbach for scientific insight and for consideration of this dissertation.

I owe much to my husband, Brian, who sustains me in hard times and champions my success in good times. May everyone have such a person in their lives. I also thank the rest of my family, especially my parents who have enabled my education and achievements at every step and my brother and sister for setting examples worth living up to. I'm fortunate to have extended and in-law family deserving of acknowledgment as well; thank you all for your inexplicable enthusiasm and assurances that you'll read this dissertation. (You may be the only ones.)

I have many friends and fellow grad students who helped make this experience endurable. Enrica Quartini has been fighting the good fight beside me until the end and I thank her for amazing Italian dinners and much-needed moral support.

Marie Cavitte has been my fellow mis-adventurer since our first AGU conference in 2010 and she has been a constant source of optimism since. Chad Greene has been a valuable sounding board about both science and life and I admire his resilience, editing skills, and interest in good flag design. Benj Wagman provided useful feedback on bad drafts along the way; I thank him for his constructive criticism and votes of confidence on my work. Noble Hatten has provided glimmers of life on the other side of graduation as well as moral support and Mexican martinis, an essential ingredient to finishing this PhD. There are countless others who have played a role in helping me reach this milestone and I thank them for their friendship, support, and diversions from the trials of grad school.

I owe more of my sanity to the Georgetown Friends than they know. They welcomed me as an old friend soon after I arrived in Austin and have continued to welcome me back even after stretches of absence due to my travel and the distractions of life. I thank them for being a family away from home and for giving me the most basic of support, including gas money and a place to sleep as well as encouragement and inspiration to not let life dictate my priorities.

Many women have set powerful examples of competence and high achievement. I acknowledge Liz Curry-Logan and Lauren Andrews in particular, who have been unwitting role models for my own perseverance.

I also thank others at UTIG who supported me in various ways, including Kaustubh Thirumalai for being an inspiration as a scientist as well as a good friend, Pedro DiNezio for material support of the work in Chapter 2 as well as for having an infectious positive attitude and joy about doing science, and Kathy Ellins who shared with me everything from her home to lessons from her career experience.

This work was made possible by a small army of dedicated technical support people who tirelessly work behind the scenes to make science happen. I can't say enough about Mark Wiederspahn's commitment to making the world a better place, though I'm not sure he thinks of it that way. As I struggled against countless hardware and software gremlins, he reminded me "when you're on the bleeding edge, you bleed a lot". He was always there to stave off the bleeding. Penelope Parr is a Landmark guru who taught me things I never knew I never knew and readily made my life easier. I also appreciate the perseverance of anyone and everyone at the Texas Advanced Computing Center who responded to one of my countless support tickets, a thankless job. Of the TACC staff, I owe most of my gratitude to Greg Abram, who constantly amazed me with his availability and willingness to patiently teach me VTK skills (and fix my bugs) while making it sound like he was having fun. I aspire to be more like him.

I have had the pleasure of working with excellent scientific and engineering support staff at UTIG both in Austin and in the field. Greg Ng and Scott Kempf have had limitless patience for dumb questions and lengthy explanations. I thank Tom Richter for sharing his wisdom, telescope, and pure love of theoretical math as well as for teaching me that better is the enemy of good enough (but only sometimes).

The world-class administrative staff at UTIG have also supported this work in more ways than I could count, including handling so much of the behind-the-scenes work of keeping things running so I (and everyone at UTIG) could spend more time focusing on research. In particular, I thank Judy Sansom, Rosalind Gamble, and Nancy Hard who have seen me all the way through my time at UTIG.

I thank those co-authors who have not already been mentioned for valuable contributions to parts of this work, including those submitted for peer-reviewed publication. Dan Martin and Scott Waibel contributed to work in Chapter 2. Tobin Isaac and Hongyu Zhu contributed to model development and evaluation included in Chapter 4.

Summer interns from UT, other universities, and local high schools played an important role in the interpretation of data for this research. All endured grueling summers of grunt work, the true scientific experience. Interns who specifically contributed to this research include Rebekah Albach, Shubhanga Ballal, Arami Rosales, Robert Stephany, and Varun Sudunagunta.

As with any scientific endeavor, this work would not have been possible without funding. This includes funding from the UT Jackson School of Geosciences, the G. Unger Vetlesen Foundation, the UT Institute for Geophysics, the National Science Foundation, and the Department of Energy. Field work was made possible by funding from the National Science Foundation. Other support came from NASA, the Statistical and Applied Mathematical Sciences Institute, the Society for Industrial and Applied Math, the International Glaciological Society, the Texas Advanced Computing Center, and the National Energy Research Scientific Computing Center.

West Antarctic Ice Sheet Retreat during the Last Interglacial

Gail Ruth Muldoon, Ph.D.
The University of Texas at Austin, 2018

Supervisors: Charles S. Jackson
Donald D. Blankenship

The Last Interglacial (116 ka - 130 ka) is the most recent time when Earth's climate was as warm or warmer than it is today. It therefore may make a suitable proxy for understanding the impacts of modern climate change. One such impact of immediate relevance to the modern world is that of sea level rise. Global sea level is currently rising at an accelerating pace, threatening lives and economies around the world. Notably, evidence from paleoclimate data suggests global sea level during the Last Interglacial was at least 6.6 m higher than present sea level and perhaps more than 8 m higher. As the Earth adjusts to the rapid onset of modern climate change, we may expect sea level to approach that of the Last Interglacial.

Noticeable changes in sea level have a number of sources, including melting glaciers, ice sheets, and ocean thermal expansion. The Antarctic Ice Sheet has been inferred to be the largest contributor to Last Interglacial sea level change, adding between 4.1 and 5.8 m to global sea level during that time. Most of this change is expected to come from the West Antarctic Ice Sheet, which is thought to be prone to marine ice sheet instability. However, uncertain basal boundary conditions and ocean forcing make it a challenge to know how the ice sheet may have lost such a large amount of mass.

In this work, I seek to better constrain mass balance and sea level contributions of the Antarctic Ice Sheet during the Last Interglacial and explore evidence from inside the ice sheet itself which may reveal if and how the ice sheet sustained such a large mass balance change during the Last Interglacial. To do so, I use a transient ice sheet model to simulate reconfiguration of the Antarctic Ice Sheet under Last Interglacial conditions and find a stable configuration consistent with estimates of Antarctic contributions to Last Interglacial sea level. I then analyze englacial radar stratigraphy to study the ice dynamics by dating a series of isochronous englacial reflectors which have been mapped through the central West Antarctic Ice Sheet. For comparison to this data, I implement a steady state ice sheet model to simulate englacial isochronous surfaces with various uncertain model boundary conditions.

Table of Contents

List of Tables

List of Figures

Chapter 1

Introduction

1.1 The “missing ice” problem for the Last Interglacial

The Earth’s glaciers are losing mass and contributing to sea level rise at an accelerating pace in response to modern climate change. Current sea level rise is dominated by ocean thermal expansion and melting of mountain glaciers and the Greenland Ice Sheet (Bindoff et al., 2007; Dalrymple et al., 2012; World Glacier Monitoring Service, 2008). However, the Antarctic Ice Sheet is expected to experience increasing ice mass loss for the foreseeable future and contains a far larger reservoir of ice than mountain glaciers and the Greenland Ice Sheet combined (Dalrymple et al., 2012). While uncertainty remains about the extent to which the Antarctic Ice Sheet will lose mass into the ocean, earlier examples of ice sheet mass loss may provide clues of what to expect.

The last time temperatures were similar to the modern was during the Last Interglacial (LIG) about 130,000 to 115,000 years ago (Figure 1.1). Data suggests ice sheets were smaller and sea level higher at that time, changes that are also being observed today. Kopp et al. (2009) estimate a 95% probability that during the LIG global sea level was 5.9 m higher than today and a 67% probability sea level exceeded 7.2 m.[1] The most likely explanation for this sea level highstand is mass loss from ice sheets. Thermal expansion of the ocean also contributes to sea level rise, but estimates indicate only 0.4 ± 0.3 m sea level rise due to thermal expansion was likely during the LIG (McKay et al., 2011).

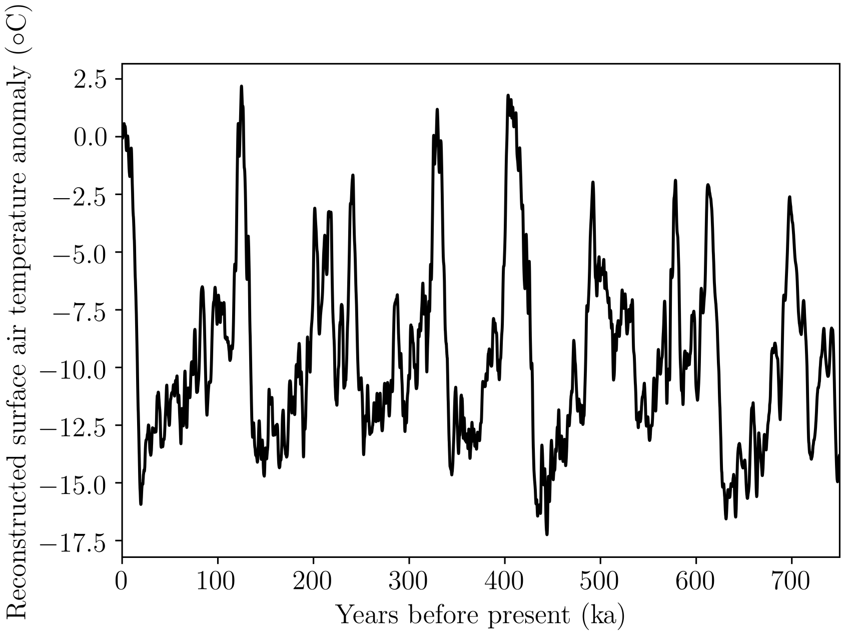

Figure 1.1: Surface air temperature anomaly above 45°N relative to the modern during the last 750 ka. This data was reconstructed by Bintanja and Van de Wal (2008). The most recent time during which temperatures were comparable to the modern occurred approximately 125,000 years ago during the Last Interglacial.

Current estimates of LIG sea level contributions from each of the major ice sheets suggest there is “missing ice” in the LIG sea level budget. The two main

---

[1] These estimates exclude erosional proxies for which timing is highly uncertain.

sources of ice melt which may have contributed to such a significantly higher sea level compared to today are the Greenland Ice Sheet (GIS) and the Antarctic Ice Sheet (AIS). Stone et al. (2013) suggest there is a 90% probability the GIS contributed more than 0.6 m to LIG sea level and less than 10% likelihood the GIS contributed more than 3.5 m. Another study by Quiquet et al. (2013) estimates GIS melt during the LIG was between 0.7 and 1.5 m sea level rise equivalent, consistent with the Stone et al. (2013) result. The thermal expansion and GIS contributions therefore are unlikely to account for more than 4.2 m sea level rise[2] during a time when sea level was likely to have been at least 5.9 m higher than today. This upper estimate suggests GIS melt could not have been solely responsible for LIG sea level rise. Therefore, the remainder of ice melt likely originated in the AIS. Estimates from paleooceanographic data and coupled atmosphere-ocean climate modeling suggest an AIS contribution to sea level rise of 4.1 to 5.8 m during the LIG (McKay et al., 2011). Collapse of the submarine-based West Antarctic Ice Sheet (WAIS) seems to be a particularly likely source of the missing sea level change. Modern observations reveal mass loss in the region and the WAIS is expected to be vulnerable to marine ice sheet instability (Joughin and Alley, 2011; Joughin et al., 2014). Simulations completed in other studies suggest deglaciation of all but the Marie Byrd Land portion of the WAIS is possible and may result in up to 3.3 m of sea level rise (Pollard and DeConto, 2009; Bamber et al., 2009). However, estimates of Antarctic Ice Sheet melt during the LIG are largely theoretical; there are currently no direct observations of widespread melting of the AIS during the Last

---

[2] This estimate includes 0.7 m sea level rise from thermal effects and 3.5 m from GIS melt.

Interglacial.

This work combines englacial ice-penetrating radar observations, observation-based boundary conditions, and steady-state simulations of the WAIS to look for evidence of ice mass loss as recent as the LIG. Simulating paleo deglaciation requires sophisticated transient models with accurate paleo boundary conditions, but such transient models and boundary conditions are not available. Instead, I compare englacial observations to the steady state scenario, assumed to be stable. Such a comparison is expected to emphasize non-steady-state characteristics of the system which may be indicators of past ice mass loss. Chapter 2 explores an approximately steady state Antarctic Ice Sheet geometry in the presence of widespread retreat that may have occurred during the Last Interglacial to find such a response is consistent with the “missing ice" budget. Chapter 3 goes on to date observed englacial radar reflectors as old as 25 ka which provide a basis for constraining the distribution of ice deposited before the Last Glacial Maximum and perhaps as long ago as the Last Interglacial. Finally, Chapter 4 uses a sophisticated steady state model to simulate englacial horizons and compare them to observed radar reflectors in an effort to quantify the sensitivity of such englacial horizons to model boundary conditions and to look for evidence of instability in deviations of observed englacial horizons from the expected steady state geometry.

1.2 WAIS Instability

The Antarctic Ice Sheet is comprised of two parts, the WAIS and the East Antarctic Ice Sheet (EAIS). I hypothesize the “missing ice” required to raise global sea level during the LIG by at least 5.9 m—and likely 7.2 m—originated in the WAIS. Paleontologic and geochemical evidence of open water conditions in the WAIS basin suggest the WAIS deglaciated at least once during the last 750,000 years, though this evidence does not show deglaciation specific to the LIG (Scherer et al., 1998). However, recent modeling efforts suggest the EAIS contributed 3–5 m to LIG sea level rise as a result of ocean warming (Fogwill et al., 2014) and additional modeling experiments indicate WAIS deglaciation precedes that of the EAIS (Pollard and DeConto, 2009).

The WAIS is a likely candidate to have contributed significantly to sea level rise during the LIG because of its susceptibility to effects from the Marine Ice Sheet Instability (MISI) hypothesis as a result of its basal configuration. The initiation of ice retreat increases the ice surface slope and leads to an increasingly thick glacial terminus due to the inland-sloping bed beneath. The surface slope and thick terminus result in accelerated ice velocity and subsequent positive feedback of accelerating mass loss through thinning and retreat (e.g. Schoof, 2007; Parizek et al., 2013).

While subglacial conditions such as bed roughness and till[3] deformation

---

[3] Till is a sediment consisting of particles of various sizes deposited by melting glaciers or ice sheets. It commonly occurs under existing glaciers and ice sheets at the ice-bed interface.

may counteract this tendency toward ice mass loss, it is not known to what extent these opposing bed conditions may act to slow deglaciation locally (Winsborrow et al., 2010; MacGregor et al., 2013). Previous work suggests the WAIS would contribute 3.3 m to LIG sea level from complete loss of unstable ice (Bamber et al., 2009)[4] and current thinning of Thwaites Glacier provides evidence for one example of an outlet for ice in the Marie Byrd Land (MBL) sector of the WAIS.

Recent observations have identified potential climate-induced tipping points in the WAIS. Evidence suggests Thwaites Glacier, a sizable WAIS outlet, underwent sustained thinning in the past few decades and is currently held back by a $\sim$50 km wide submarine topographic sill (Joughin et al., 2014). Observations of subglacial conditions suggest if the glacier retreats off the sill, deglaciation of WAIS ice grounded below sea level may follow, potentially raising global eustatic sea level by 3.3 m. Evaluation of WAIS extent during the LIG may therefore provide a gauge for what to expect from impending SLR.

Stone et al. (2003) used cosmogenic dating of bedrock exposed in MBL to explore the extent of glacial cover over the past several million years. Their work revealed current glacial extent of the WAIS is anomalously low compared to the last several million years, but MBL glaciation is similar to the minimum extent observed during the late Pleistocene. This suggests the WAIS did not deglaciate to less than

---

[4] Though the WAIS can be considered more unstable due to deeper bathymetry and it has been suggested WAIS deglaciation would precede that of the EAIS, deglaciation of both the WAIS and parts of marine-based ice in the EAIS are consistent with upper estimates of the LIG sea level rise budget.

its modern extent during the LIG. However, the analysis by Stone et al. (2003) is limited to locations of bedrock outcrops exposed by deglaciation; information about deglacial history preserved in the current ice sheet is not included. Englacial layers in the WAIS may reveal additional information about the pattern of deglaciation and bring a deeper understanding of LIG mass balance trends.

1.3 Challenges of finding “missing ice”

As in other paleoclimate problems, models are needed to evaluate the state of the WAIS during the LIG because of the lack of observations during that time and the complexity of the interacting physical systems. However, our ability to model ice sheets, though advancing rapidly, is limited. For example, few existing models are capable of including englacial layers which may be the key to investigating nuanced changes in ice flow indicative of past ice sheet behavior. This work uses the recently-developed Ymir ice sheet model (Isaac et al., 2015) that is capable of producing a three-dimensional velocity field, which can be used to simulate the englacial age of ice for comparison to observations. Though we do not use the model to represent transient ice flow, the steady state case allows for adequate testing of the null hypothesis that the WAIS did not deglaciate during the LIG.

A complicating factor in this analysis is that ice sheet models depend on accurate boundary conditions to represent the physical world. All boundary conditions contain errors, just as all observations do, but the issue is compounded by the inaccessibility of the base of an ice sheet. Fields such as basal topography, traction, and geothermal flux are directly or indirectly observable, but only on discrete grids and often with large errors due to the complexities introduced by the presence of as much as 3 km of overlying ice. Large errors in these boundary conditions may reduce the signal to noise of modeled geometry and age of deep ice in such a way that limits our ability to interpret paleo ice flow dating back to the LIG. Additionally, poor error analysis and/or reporting may ignore spatial correlation of errors, making it difficult to sample boundary condition uncertainty. To mitigate these issues, the most recent data-constrained basal boundary conditions are used to constrain Ymir simulations.

1.4 Identifying Last Interglacial ice

One method to evaluate whether the WAIS deglaciated during the LIG is to examine the distribution of what was deposited during that time and still remains in the ice sheet. However, frictional heating from more recent ice flow, such as through the Siple Coast and Amundsen Sea Embayment ice streams and outlet glaciers, may have erased much of the deep, old ice at the ice-bed interface. Additionally, the WAIS is underlain by the West Antarctic Rift System (WARS) which leads to elevated geothermal fluxes in the region that may promote basal melting (Blankenship et al., 1993; Schroeder et al., 2014). It is therefore necessary to simulate targets for the search for Last Interglacial ice and to consider the implications of where it is and is not found. Chapter 2 includes experiments related to the expected location of surviving ice in the event of LIG collapse.

I hypothesize the most likely location for the preservation of old ice is in the highlands of Marie Byrd Land (MBL), where higher elevations may have remained cold enough for ice to persist through the LIG and where ice flow is minimal due to topographic barriers. Recent observations of this area by the University of Texas Institute for Geophysics provide information about englacial isochronous ice layers which can be dated in relation to WAIS ice cores. However, direct dating of englacial layers is only possible in relation to ice cores that are within the airborne radar survey area. While Last Interglacial ice may have already been detected in West Antarctica (N. Ross, pers. comm., 2014), it is outside the survey area. The oldest dated ice within the survey area is 90 ka at Byrd Station (Blunier and Brook, 2001). As described in this analysis, available ice-penetrating radar observations in the WAIS which have been tied to the Byrd and WAIS Divide ice cores are only as old as 25 ka. While these reflectors provide constraints on the age of the ice beneath the deepest observable reflector, they do not reveal the presence of LIG ice.

Even without directly identifying LIG ice, the configuration of englacial layers in the MBL highlands may provide evidence for the presence or absence of ice in the WAIS basin during the LIG. The flow direction of old ice, manifested in deformation of overlying layers, may reveal if the ice sheet persisted or if the WAIS submarine basin was inundated by ocean water at some time during the last 125,000 years. Evidence of ice disruption or deformation older than the Last Glacial Maximum 21,000 years ago may be indicative of deglaciation during the LIG. The oldest reflector dated in Chapter 3 may therefore provide such information.

1.5 Englacial isochrones

Isochronous englacial horizons effectively record ice flow history. As snow is compacted into ice by gravity and undergoes strain thinning as a result of ice flow, depositional events appear to be roughly horizontal horizons in the ice column (Figure 3.2) which are generally assumed to be isochronous (Vaughan et al., 2004). Seasonal deposition of snow incorporates dust and aerosols from the present atmosphere, which modify dielectric properties of the horizons. Contrasts in dielectric properties lead to reflections in ice-penetrating radar.

Englacial isochrones in the Thwaites Glacier catchment were surveyed using airborne ice-penetrating radar instruments as a part of laterally-extensive surveys covering much of the central WAIS (Figure 3.1). Radar sounding data were collected mostly on a 15 km × 15 km grid using the 60-MHz High-Capability Radar Sounder (HiCaRS; Peters et al., 2007) for the Airborne Geophysical Survey of the Amundsen Sea Embayment (Holt et al., 2006, AGASEA, collected 2004) and HiCaRS2 (Young et al., 2016) for the Geophysical Investigations of Marie Byrd Land Evolution (GIMBLE; Young et al., 2017) projects. Coherent radar data were focused using synthetic-aperture radar (SAR) processing techniques to better resolve englacial and subglacial features (Peters et al., 2007). Earlier incoherent radar surveys (CASERTZ, SOAR/WMB; Morse et al., 2002; Luyendyk et al., 2003) were also included to extend data coverage, though the reflector quality is lower.

Continuous reflectors in post-processed radargrams with flattened surfaces are tracked for hundreds of kilometers in the Thwaites Glacier catchment using a semi-automated method employed by the seismic imaging software *Landmark*.

Where the radar survey crosses near an ice core, ages derived from isotopic dating of the ice core are assigned to englacial reflectors as in Chapter 3. These data are independent of observations currently being used to tune and calibrate existing models, which means it is possible to make a meaningful comparison between modeled and observed layers for the purpose of hypothesis testing.

The shape and distribution of englacial reflectors can deviate due to topographic effects, variable accumulation, or changes in ice flow. Layer drawdown may mark the presence of anomalous geothermal heat and/or activation of fast flow such as in an ice stream (Leysinger Vieli et al., 2007; Cavitte et al., 2013b). Folding of englacial layers is also possible as a result of inhomogeneities in ice rheology (Waddington et al., 2001; Thorsteinsson and Waddington, 2002). Such signatures of past ice flow are useful for interpreting the behavior of paleo ice sheets, even in the absence of Last Interglacial ice, as they may affect the pattern of later layer deposition. Chapter 4 demonstrates the simulation of englacial isochronous surfaces for a range of model boundary conditions and discusses model limitations restricting the interpretation of the surfaces presented.

1.6 Ice sheet models and uncertainty

Ice sheet models make assumptions about the physics governing ice flow as well as the boundary conditions and climate forcings acting on an ice sheet. Recent model development has led to greater sophistication in these models, but errors still exist and are expected to contribute to uncertainty in modeled ice sheet geometry and volume. Model accuracy is often defined in reference to available observations. Model-data discrepancies are computed to determine how well models represent the observed state of a physical system such as an ice sheet. For example, discrepancies between modeled and observed englacial isochrone depth arise due to imperfect knowledge of ice flow physics and/or model boundary conditions.[5] I seek to separate these effects using sensitivity analysis in Chapter 4 to isolate model-data discrepancies due to uncertain boundary conditions as opposed to discrepancies due to deviations of observations from steady state flow (as simulated). The thermomechanical Ymir ice sheet model (Isaac et al., 2015) used in this analysis uses adjoint methods to efficiently solve the Full Stokes equations of ice flow in three dimensions. This high-fidelity model is among the best available steady state ice sheet models.

Several techniques have been used to better surmise basal boundary conditions from available observations. Inversion of basal traction and temperature from surface ice velocity, geometry, and accumulation ensure self-consistency (e.g. Morlighem et al., 2013; Petra et al., 2012; Zhu et al., 2016). Spatial statistical techniques have been used to interpolate subglacial topography at high resolution between survey lines (Goff et al., 2014). Finally, heterogeneous geothermal flux has been deduced from analysis of water distribution based on the radar reflectivity at the ice-bed interface (Schroeder et al., 2014). This work includes these cutting-edge

---

[5] Observations of horizons are also imperfect and therefore have associated uncertainty; for example, uncertainty in the age of observed englacial reflectors generally increase with depth, but is strongly dependent on the signal to noise ratio of individual reflector detection.

results in an effort to realistically represent the uncertain ice sheet basal boundary.

1.7 Scope of Work

I hypothesize the unstable WAIS is the most likely source of the “missing ice" observed in paleoclimate records of the Last Interglacial sea level highstand. To examine evidence of collapse of the WAIS during this time, I combine observational analysis and numerical modeling capabilities described in this analysis.

Chapter 2 (Muldoon et al., 2018a, in review) uses the BISICLES ice sheet model (Cornford et al., 2013) and Community Earth System (CESM; Deser et al., 2006) to simulate the distribution of ice that would survive a LIG collapse and therefore may still be observable in the modern ice column. BISICLES is used to simulate a realistic progression of WAIS collapse due to sub-shelf melting. CESM is used to compute atmospheric circulation consistent with the lowered surface geometry of the WAIS in the event of a collapse. As expected, there are large anomalies in atmospheric temperature and precipitation at the ice sheet surface after collapse. Several sub-shelf melting conditions are applied to test the sensitivity of the ice sheet extent to a range of ocean forcings representing various extremes the ice sheet may have experienced during the LIG. The result suggests stabilization of the ice sheet volume occurs when $\sim$1 meter per year of subshelf melting is applied, but re-advance of the ice sheet grounding line is modest even with a low 10 cm subshelf melt per year, far below measurements of modern subshelf melt rates. Still, areas of the WAIS persist in the MBL region as supported by other studies (Pollard and

DeConto, 2009; Holschuh et al., 2014).

Chapter 3 (Muldoon et al., 2018b, in review) applies a statistical technique to date englacial radar horizons to determine if LIG ice is evident in the central WAIS basin. While previously-observed horizons in this dataset are not as old at the Last Interglacial, this work does not rule out the possibility that LIG ice resides in the echo-free zone near the base of the ice sheet (Fujita et al., 1999). As such, our dating analysis bounds the depths at which LIG ice may be observed in these areas. This work includes a sophisticated uncertainty analysis and reveals uncertainty in radar observations limits our ability to assign ages to englacial reflectors.

Chapter 4 demonstrates the ability to compare observed englacial reflectors with steady state reflectors simulated using the sophisticated Ymir ice sheet model (Isaac et al., 2015). It is hypothesized that discrepancies between observed reflectors and steady state simulated reflectors suggest areas of the ice sheet that are out of steady state and may be particularly prone to retreat. However, the distribution and geometry of simulated reflectors are also influenced by the choice of ice sheet model boundary conditions. To determine the extent to which discrepancies between observations and models can be explained by uncertainty in model boundary conditions, we perform a series of experiments of simulated reflector geometry using different combinations of basal topography and geothermal flux boundary conditions. This analysis includes preliminary results of simulated isochronous surfaces. This work includes additional model functionality (beyond that described in Isaac et al. (2015)) for higher vertical resolution, optimization of surface vertical velocities, and thermocoupling. However, additional model development is necessary to improve vertical resolution and model efficiency for deriving a physically justifiable 3D velocity field from which simulated isochronous surfaces can be derived.

Chapter 2

Configuration and sea level contribution from the Antarctic Ice Sheet during the Last Interglacial

Evidence shows sea level was at least 6.6 m higher and likely exceeded 8.0 m during the Last Interglacial (130 - 116 ka), but accounting for the source of such a large sea level change has been challenging. Contributions from the Greenland Ice Sheet, ocean thermal expansion, and mountain glacier mass loss are not sufficient to account for the difference and so it is expected ice mass loss from the Antarctic Ice Sheet contributed at least half of this sea level change. However, the distribution of this mass loss is not known.

We simulate aspects of reduced volume of the Antarctic Ice Sheet using Last Interglacial conditions at 121 ka with an imposed warming of the ocean to investigate the geometry of a reduced configuration ice sheet and to identify areas of ice that persist through such an event. We estimate the environmental response to a lowered West Antarctic Ice Sheet as well as associated anomalies in ice sheet surface mass balance. To account for a potential range of climates during the LIG, we perform experiments with a range of subshelf melting to determine the configuration in which the ice existed.

Our results suggest the sea level contribution of the Antarctic Ice Sheet may have stabilized at 4.56 m with a subshelf melt rate of 1 m/a during the Last Interglacial. However, higher melt rates (20 m/a) similar to those resulting from exposure to modern circumpolar deep water result in at least 5.3 m sea level rise. On the other hand, relatively low melt rates (10 cm/a) suggest a contribution less than 4.05 m. These values are consistent with estimates of ice mass loss that are otherwise unaccounted for in the Last Interglacial sea level budget.

2.1 Introduction

The West Antarctic Ice Sheet (WAIS) is potentially susceptible to large-scale thinning and retreat and observations of recent mass loss give added concern that such a reconfiguration may already be underway. A similar reconfiguration may have occurred as recently as the Last Interglacial (LIG; 130 to 116 ka), however direct evidence is lacking. Sea level estimates for the LIG suggest a 95% probability that sea level was more than 6.6 m higher than today and a 67% probability the difference exceeded 8.0 m (Kopp et al., 2009). Accounting for the source of this sea level rise suggests an Antarctic Ice Sheet (AIS) contribution between 4.1 and 5.8 m (McKay et al., 2011). Collapse of the submarine-based WAIS seems to be a particularly likely source of the missing sea level change in light of modern observations of mass loss in the region and the expected vulnerability of the WAIS to the marine ice sheet instability hypothesis. Earlier estimates suggest a WAIS collapse could contribute up to 3.3 m of sea level rise (Bamber et al., 2009; DeConto and Pollard, 2016).

Marine ice sheets that reside in interior-sloping geometries are potentially subject to the marine ice sheet instability hypothesis. However, such retreat can end on localized forward-slope geometry where forces balance. It is nontrivial to estimate alternative ice sheet configurations where this occurs because of the potential for lateral and vertical stabilization of the ice flow. To explore how the AIS contributes to sea level changes during the LIG, we estimate the most stable, and therefore most likely, configuration following widespread retreat.

To search for stable configurations of the AIS, we first use a high melt rate to induce a reconfiguration of the ice sheet as described in Section 2.2. This configuration results in a dramatically lower surface elevation in the WAIS that is expected to alter the local surface mass balance. To account for this, in Section 2.3 we recalculate AIS surface mass balance in equilibrium with the new configuration. We then apply a series of decreasing subshelf melt forcings along with the recalculated surface mass balance to look for the most likely ice sheet configuration in the retreated state.

2.2 Inducing Ice Sheet Reconfiguration

We use the BISICLES ice sheet model (Cornford et al., 2013) to simulate our initial reduced-configuration Antarctic Ice Sheet (AIS) by imposing a large amount of subshelf oceanic melt for 1000 model years. The model includes an adaptive mesh down to 1 km with a subgrid-scale friction scheme which has been demonstrated to be sufficient resolution for Antarctic marine ice sheet dynamics

(Cornford et al., 2016). Boundary conditions for the model include Arthern et al. (2006) surface accumulation and basal topography based on the Bedmap2 dataset (Fretwell et al., 2012) that has been modified to respect mass conservation (Cornford et al., 2016). A thickness-dependent subshelf melt rate is applied such that there is no melting of ice less than 100 m thick or in cells with partially-grounded ice. Elsewhere, melt increases linearly up to 400 m/a for ice more than 800 m thick (Cornford et al., 2016). This unrealistically-high melt rate is used to accelerate ice sheet response to rapidly arrive at the retreated state. The ice mask remains unchanged, with an imposed minimum ice thickness of 10 m for numerical convenience.

As seen in Figure 2.1, significant subshelf melting around the AIS leads to retreat and extensive ice mass loss in the WAIS. Retreat is largely limited to areas of the WAIS with a reverse bed slope. Effects elsewhere are limited to the coastal regions of the East Antarctic Ice Sheet (EAIS) along the Oates / George V Coast and near Totten Glacier. Higher surface elevations persist in the coastal Marie Byrd Land (MBL) area and in the Ellsworth Mountains region near the Filchner-Ronne Ice Shelf.

2.3 Retreated-WAIS surface mass balance

Antarctic Ice Sheet mass balance is determined by net surface accumulation and ice flow dynamics. The BISICLES model (Cornford et al., 2013) is used to simulate ice sheet dynamics, but a climate model is needed to infer changes to surface mass balance that can then be used as external forcing by the ice sheet model. To account for the effects of significant changes in ice elevation on surface mass balance, we use the Community Earth System Model (CESM; Hurrell et al., 2013) to recompute surface mass balance. CESM is run with coupled ocean, atmosphere, land, and sea ice models. The global topography is kept the same as modern day topography except over Antarctica, where the lowered AIS surface topography is upscaled to the 2° CESM resolution.

Lowering the WAIS surface by more than 2 km in places dramatically impacts the surface mass balance in the region. Two CESM control runs were performed using modern AIS surface elevation for comparison to our experimental results. The first used modern orbital geometry and CO_2 (284.7 ppmv) while the second used the higher-eccentricity Last Interglacial (121 ka) orbital geometry and CO_2 (270 ppmv). The temperature distribution for the two control runs is similar and resembles the ice sheet's surface elevation profile with warmer temperatures corresponding to lower surface elevation. However, the modern control is up to 2°C warmer than the reconfigured case along the Antarctic Peninsula and over the Filchner-Ronne Ice Shelf while it is up to 1°C cooler over the Ross Ice Shelf. Total surface precipitation from the modern control was similar to the pattern and magnitude of surface accumulation estimated by Arthern et al. (2006).

Equilibrium 2-meter air temperature and total precipitation anomalies relative to the modern control are shown in Figure 2.2. Positive temperature anomalies over the WAIS are dominated by lapse rate effects from lowering the ice sheet surface rather than by changes in advection. We see increased temperatures of up to

7°C, but on average austral summer temperatures remain below freezing. Localized warming of ~5°C is also observed in the area of the Oates / George V Coasts in East Antarctica. Temperature anomalies elsewhere are less than 1°C, within the limits of natural variability.

The precipitation anomaly shows variations of up to ± 35 cm/yr due to surface lowering with up to 100% increase in the WAIS basin compared to modern precipitation. This is in response to surface elevation lowering and the corresponding weakening of katabatic winds (Figure 2.3) on the WAIS basin ice shelf which allows for convergence of moist air within the WAIS interior. The increased precipitation could enable a re-advance of the ice sheet grounding line in the most retreated areas. On the other hand, precipitation is reduced along the Amundsen and Bellingshausen Sea coasts compared to high modern values. This area is largely grounded above sea level and therefore does not experience as much lowering even in the case of considerable WAIS ice mass loss, such that it does not experience increased precipitation due to lapse rate effects from surface lowering. Precipitation anomalies over East Antarctica are considerably smaller than over the WAIS, but compared to nominally low modern precipitation and given the large spatial extent of the EAIS, they can still impact ice volume changes in aggregate over long adjustment timescales. Precipitation simulated using modern topography with Last Interglacial parameters is similar to that estimated by the modern control run which suggests elevation changes dominate over orbital effects.

2.4 Exploring alternate AIS configurations

In order to determine alternate configurations of the Antarctic Ice Sheet, we perform experiments to test the effect of ocean forcing via subshelf melt rates on the retreated ice sheet. In these experiments, subshelf melt rates are applied starting from the retreated state of the ice sheet in Figure 2.1B. These melt rates are spatially constant and are applied to all floating ice except in cells with partially-grounded ice. Each experiment was run for a different number of model years according to its progress, as seen in Figure 2.4. Unlike during the initial AIS reconfiguration when only ice thicker than 100 m experienced subshelf melt, ice thicker than 10 m is subject to the constant melt rate in each of our experiments. This reduces the number of large ice cliffs at calving fronts, but results in an elevated rate of ice mass loss at the start of the experiments while the ice adjusts to this change. However, there is no noticeable effect on ice Volume above Flotation (VaF) during this adjustment, suggesting the change is almost entirely due to ice self thinning with minimal dynamic impact from this phase.

Our experiments demonstrate the effects of a series of decreasing subshelf melt rates on possible retreated ice sheet configurations. In the first experiment, we assume a high 20 m/yr subshelf melt rate that is on the order of melt being experienced by floating ice in the Amundsen and Bellingshausen Sea regions exposed to circumpolar deep water (Turner et al., 2017; Holland et al., 2010). While grounding line re-advance in the basin is expected to be slower under these conditions, ice may still persist over topographic pinning points from which grounded ice can advance. However, for the duration of this 1000 year run, the grounding lines continued to retreat (Figure 2.4). The second experiment applied a 1 m/yr subshelf melt rate, which is expected to approximate moderate to low heat flux from ice-ocean interactions and is comparable to maximum accumulation rates simulated over the WAIS. The ice sheet volume and grounded area in this experiment stabilized in a similar configuration to the initial collapsed state after $\sim$1000 years and then remained steady for an additional 500 years of the model run. Grounding lines did not re-advance into the WAIS basin in either of these experiments, indicating ice sheet re-advance would require an ocean forcing less than 1 m/a.

To test a subshelf melt rate that would allow for grounding line advance, an additional experiment was performed with a 10 cm/a subshelf melt rate starting from when the 1 m/a experiment stabilized (model year 2000). In the 10 cm/a melt rate experiment, the ice sheet volume grew while the grounded area extent of the ice sheet increased roughly linearly. Ice volume increase in this experiment is roughly evenly split between the WAIS and the EAIS, which is especially notable considering the great size disparity between the two regions. In response to this low subshelf melting, the WAIS regained $\sim$10% of the modern WAIS grounded area and thickened considerably (Figure 2.5).

Differences in the resulting WAIS configuration between experiments are primarily seen around the existing icecaps in Marie Byrd Land and Ellsworth Land. The extent of ice persisting along the Bellingshausen Sea Coast was sensitive to the ocean forcing applied, with noticeable grounding line advance in the 10 cm/a melt rate experiment. Differences around the Marie Byrd Land icecap are minimal, but showed sensitivity to the position of topographic pinning points enabling grounding line advance. In particular, ice shelves are minimal thickness everywhere in the 20 m/a melt experiment, but thickening in areas of ice streaming is evident in the 1 m/a melt experiment, while the 10 cm/a melt experiment exhibits widespread thickening of the WAIS basin ice shelf and some advance of the grounding line into the basin on the interior side of the MBL highland. Additional progressive grounding line expansion in the lower melt experiments can be seen in the area of the Pine Island Glacier and interior side of the icecap in Ellsworth Land.

We computed the sea level rise equivalent associated with each of our experiments to explore which configurations may be consistent with estimates of the Last Interglacial sea level budget. After 1000 model years with constant 20 m/a subshelf melt rate, the sea level equivalent due to change in ice VaF in our model was $\sim$ 5.4 m and the AIS continued to lose mass. Of this overall sea level change, 3.2 m sea level equivalent comes from mass loss in the WAIS (see Appendix), primarily during the initial reconfiguration of the ice sheet. The remainder of the sea level contribution comes from the EAIS where only half of the mass loss occurs during the initial reconfiguration with the other half occurring during the melt rate experiments. This is likely because the initial reconfiguration quickly retreats the WAIS while the EAIS retains additional vulnerable grounded ice which can contribute to sustained sea level rise at later times. This is consistent with the expectation that WAIS mass loss precedes that of the EAIS (Pollard and DeConto, 2009). Sea level equivalent from the 20 m/a melt rate experiment is therefore consistent with upper estimates of Last Interglacial sea level, though the model integration was discontinued before coming into equilibrium.

The 1 m/a melt rate experiment was the only one to come into equilibrium during the integration time. After 1500 model years, the ice VaF stabilizes at 4.4 m sea level equivalent from the AIS with 1.2 m contribution from the EAIS and 3.1 m originating in the WAIS (Figure 2.6). The latter is consistent with estimated sea level contribution from the WAIS suggested by Bamber et al. (2009) and this overall sea level contribution is consistent with estimates of the AIS contribution to global sea level change during the Last Interglacial (McKay et al., 2011).

Beginning from the stability point of the 1 m/a melt experiment, forcing with subshelf melting of 10 cm/a shows continuing increase in the ice VaF, ending in 4.0 m sea level equivalent below the modern ice sheet after 1000 model years. This includes a 1.0 m contribution from the EAIS and 2.9 m from the WAIS. This sea level rise equivalent is below estimates of AIS contribution to global sea level during the Last Interglacial and is continuing to decline when the model integration is terminated. This experiment is therefore unlikely to represent an ice sheet configuration consistent with sea level observations from the Last Interglacial.

2.5 Discussion

Our model and boundary conditions exclude some features which we do not expect to impact our results. We do not incorporate the cliff-failure mechanism identified by Pollard et al. (2015) that has been proposed as an important driver of ice sheet retreat. However, we expect this mechanism is not relevant in our simulations because the model sufficiently resolves grounding line dynamics in our experiments while maintaining a minimal ice shelf such that large cliffs at the ice front do not form. Additionally, use of the Bedmap2 basal topography boundary condition does not include the latest observations from airborne ice-penetrating radar in Marie Byrd Land (Young et al., 2017); however we do not expect this to make a noticeable difference in the results because the updated topography does not appear to make the ice sheet more sensitive to ocean-induced retreat (Holschuh et al., 2014). Despite these potential shortcomings, the reduced configuration ice sheet we compute is similar to the equilibrium AIS under extreme interglacial forcing with a 10 m/a subshelf melt rate for exposed and deep sea areas estimated by Pollard and DeConto (2009). This suggests our model reasonably simulates AIS retreat for the Last Interglacial.

The subshelf melt rates used for the experiments in this study are meant to represent a range of possible values experienced by the ice shelves during the LIG. The 20 m/a melt rate is high by modern standards and today occurs only in localized areas where the CDW shoals on the continental slope. It is unknown what subshelf forcing might have been applied to the LIG ice sheet, but ocean warming of 2°C may be sufficient to approach subshelf melt rates of 20 m/a (Holland et al., 2008). As a result, widespread warming of the oceans during the LIG may have resulted in a high melt rate everywhere under the AIS ice shelves as is simulated in our experiment.

The 1 m/a melt rate is comparable to accumulation rates simulated for the LIG WAIS and therefore may not be expected to exceed positive mass balance in the WAIS from surface accumulation and convergence of ice in the basin. However, this experiment results in a near-equilibrium rather than grounding line advance, while a melt rate between 10 cm/a and 1 m/a is necessary for even moderate ice regrowth. This suggests that in order for the WAIS to re-advance from a retreated LIG state to its modern configuration, subshelf melt rates were not likely to have been as high as those observed today along the Amundsen Sea Coast (Pritchard et al., 2012) despite significant retreat and coastline expansion in the WAIS. This may be due to ice sheet grounding-line hysteresis, in which it is difficult to advance the grounding line from a stable position (Schoof, 2007). The lack of grounding line advance in our simulations may be mitigated by glacioisostatic adjustment, which is left out of our model but would have made the WAIS basin less deep and therefore easier to for the ice to advance.

For these experiments, the ice mask does not change during ice sheet retreat; as the grounding line retreats, a 10 m thick ice shelf remains in areas that may otherwise be open water. In leaving these areas ice covered, we assume there is no change in the global surface albedo, which simplifies atmospheric modeling efforts. Though it may be unrealistic to assume the ice cover remains exactly the same, it is reasonable to assume an ice shelf or sea ice would persist in this area. We also do not account for additional exposure of ice to ocean forcing as sea level rises. However, ocean siphoning is expected to more than compensate for this locally as the global distribution of mass (and therefore sea level) moves away from the AIS in response to ice sheet mass unloading (O'Leary et al., 2013). Glacioisostatic rebound may also counter the net effect of local sea level change, though our model also does not incorporate such rebound. The net effect of these opposing factors is unclear.

2.6 Conclusion

We found grounding line position in this reconfiguration is relatively insensitive to ocean forcing and surface mass balance changes, suggesting our results represent a stable reconfiguration of the AIS in the event of LIG retreat. The reconfigured WAIS geometry simulated by our model is representative of a widespread LIG ice mass loss, though the pace at which we induce ice mass loss is unrealistically rapid. Our results show the WAIS retreats more readily than the EAIS, as has been shown previously by other models (e.g. Pollard and DeConto, 2009) and is expected due to the bed geometry under the WAIS.

In all of our experiments, ice persists in the Marie Byrd Land highlands and coastal Ellsworth Land. Ice also remains in the Ellsworth Land highlands and on parts of the Antarctic Peninsula. We expect this pattern of retreat would leave evidence where englacial ice deformation was influenced by flow direction change due to the creation of coastline on the inland side of the isolated icecaps.

Our 1 m/a subshelf melt rate experiment approaches equilibrium mass balance when sea level equivalent mass loss is 4.5 m, including contributions of 3.1 m and 1.2 m from the WAIS and the EAIS, respectively. This is consistent with estimates of sea level differences expected of the AIS which cannot be accounted for by other sources, suggesting hypotheses of WAIS retreat during the LIG are reasonable. Following WAIS retreat, the EAIS remains somewhat sensitive to high subshelf melt rates even as the rate of WAIS ice mass loss above flotation slows. We find regrowth from this deglaciated state requires an ocean forcing corresponding to less than 1 m/a subshelf melt, with 10 cm/a subshelf melt forcing showing gains in mass balance. This result suggests the WAIS may not easily regrow, even on existing pinning points, unless subshelf melt rates are comparable to or less than accumulation rates in the area.

2.7 Supplemental Information

Sea level rise contributions from each ice sheet were computed from change in volume above flotation for the east and west portions of the Antarctic Ice Sheet. ICESat drainage basins (Zwally et al., 2012) were used to define these regions. Values attributed to the WAIS include the Antarctic Peninsula, covering basins 1 and 18 – 27. The remainder of the basins (2 – 17) were considered part of the EAIS.

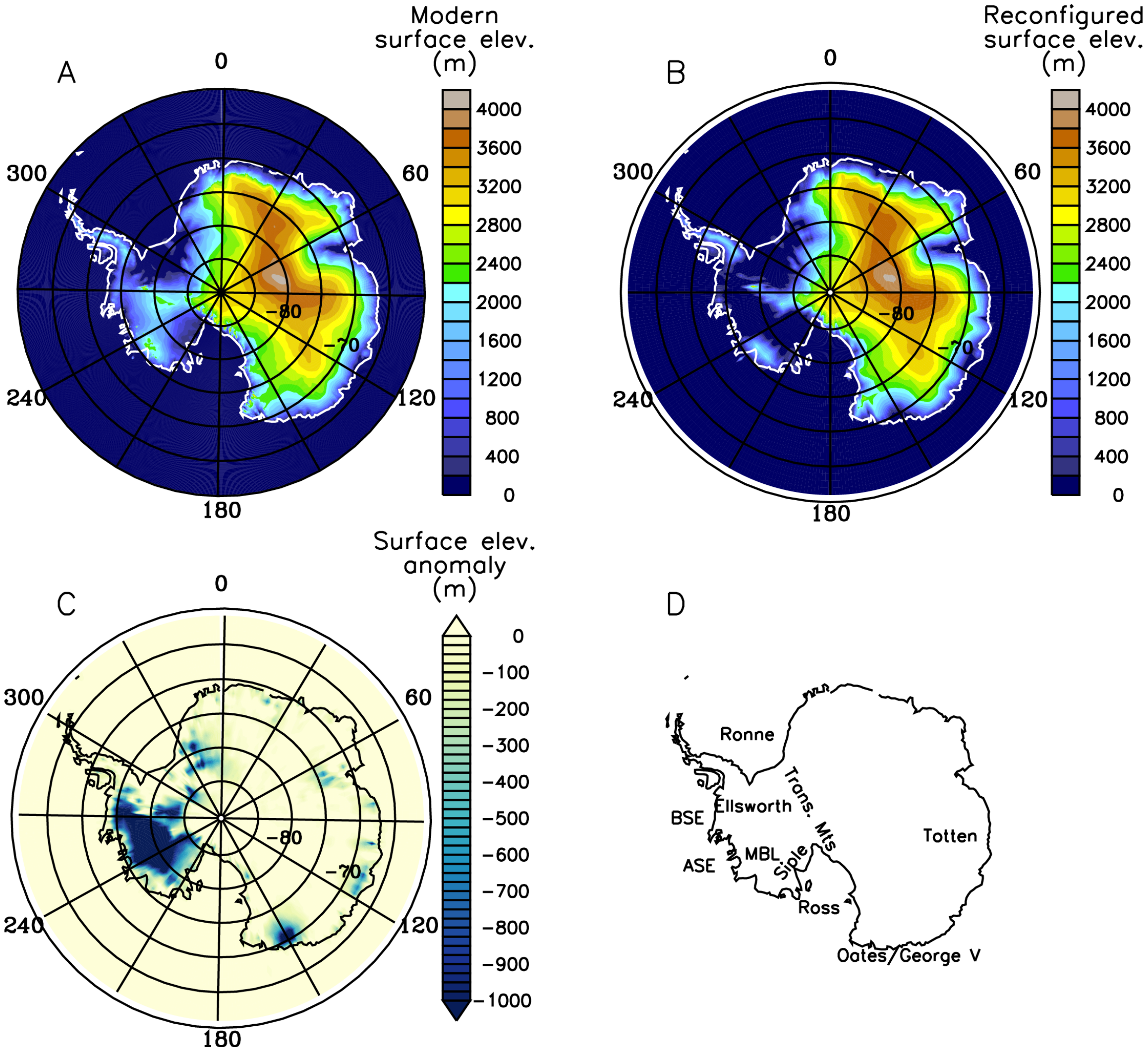

Figure 2.1: A) Ice surface topography of the modern Antarctic Ice Sheet. B) Ice surface topography simulated by the BISICLES model using high melt rate forcing (Cornford et al., 2016) to reconfigure the ice sheet to a retreated state. C) Anomaly between the modern and retreated ice sheet configuration. D) Location references of features mentioned in the text.

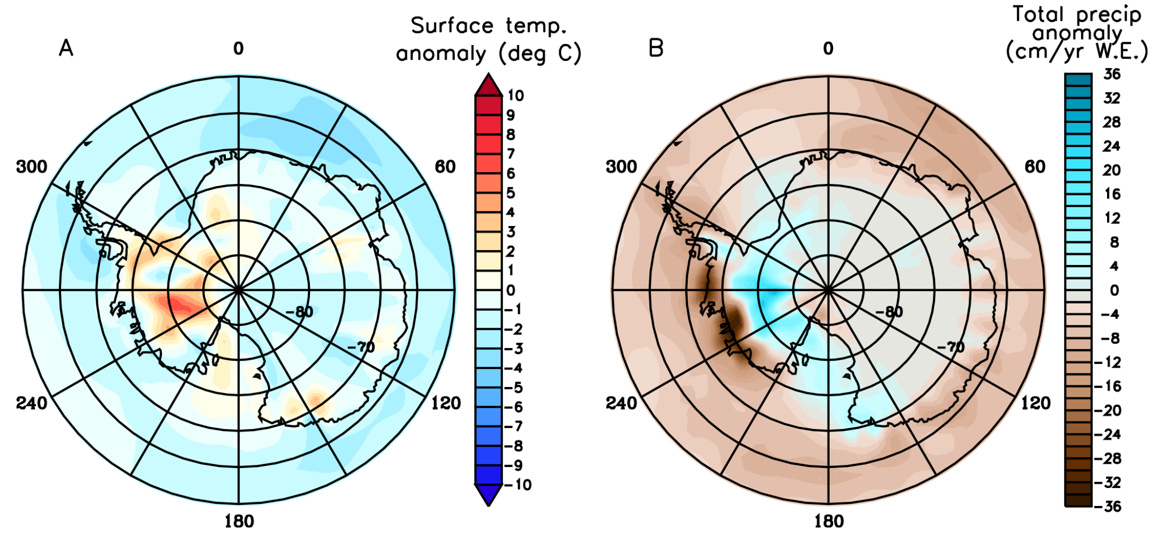

Figure 2.2: Simulated A) temperature and B) precipitation anomalies between lowered and modern ice surface scenarios. Considerable differences can be seen over the WAIS where temperatures increase as expected due to lapse rate effects in the WAIS basin. Precipitation anomalies are up to ± 35 cm/a in the WAIS while there is little effect on the EAIS.

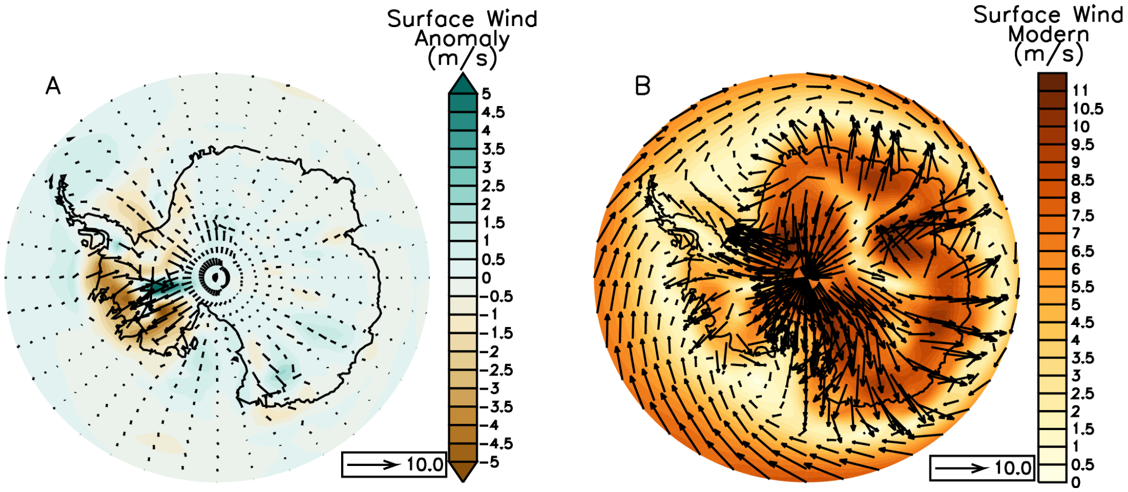

Figure 2.3: A) Change in surface wind speed and direction due to lowering of topography resulting from Last Interglacial grounding line retreat. Negative values indicate weakening of winds due to ice sheet retreat. Large changes to circulation are seen over the WAIS, bringing increased moisture from the Southern Ocean into the WAIS basin. B) Wind circulation over modern WAIS topography with Last Interglacial boundary conditions from which the anomaly was derived.

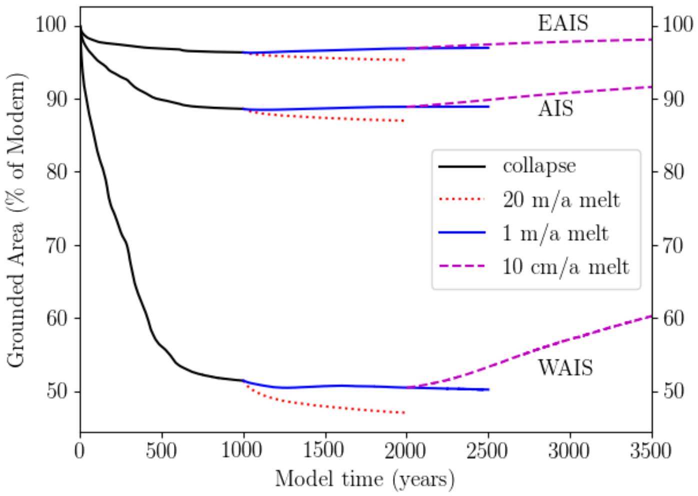

Figure 2.4: Area of grounded ice extent of the Antarctic Ice Sheet for each subshelf melt rate experiment. In the 1 m/a melt rate case (blue dashed line), grounded area begins increasing before appearing to stabilize, at which point the 10 cm/a melt experiment (magenta dotted line) is initiated. The 20 m/a experiment (red dash-dotted line) shows a steady decline and the 10 cm/a experiment shows steady increase in grounded ice extent. The initial retreat run (black line) shows the evolution of the ice sheet from the modern (at time 0) to the lowered topography as in Cornford et al. (2016).

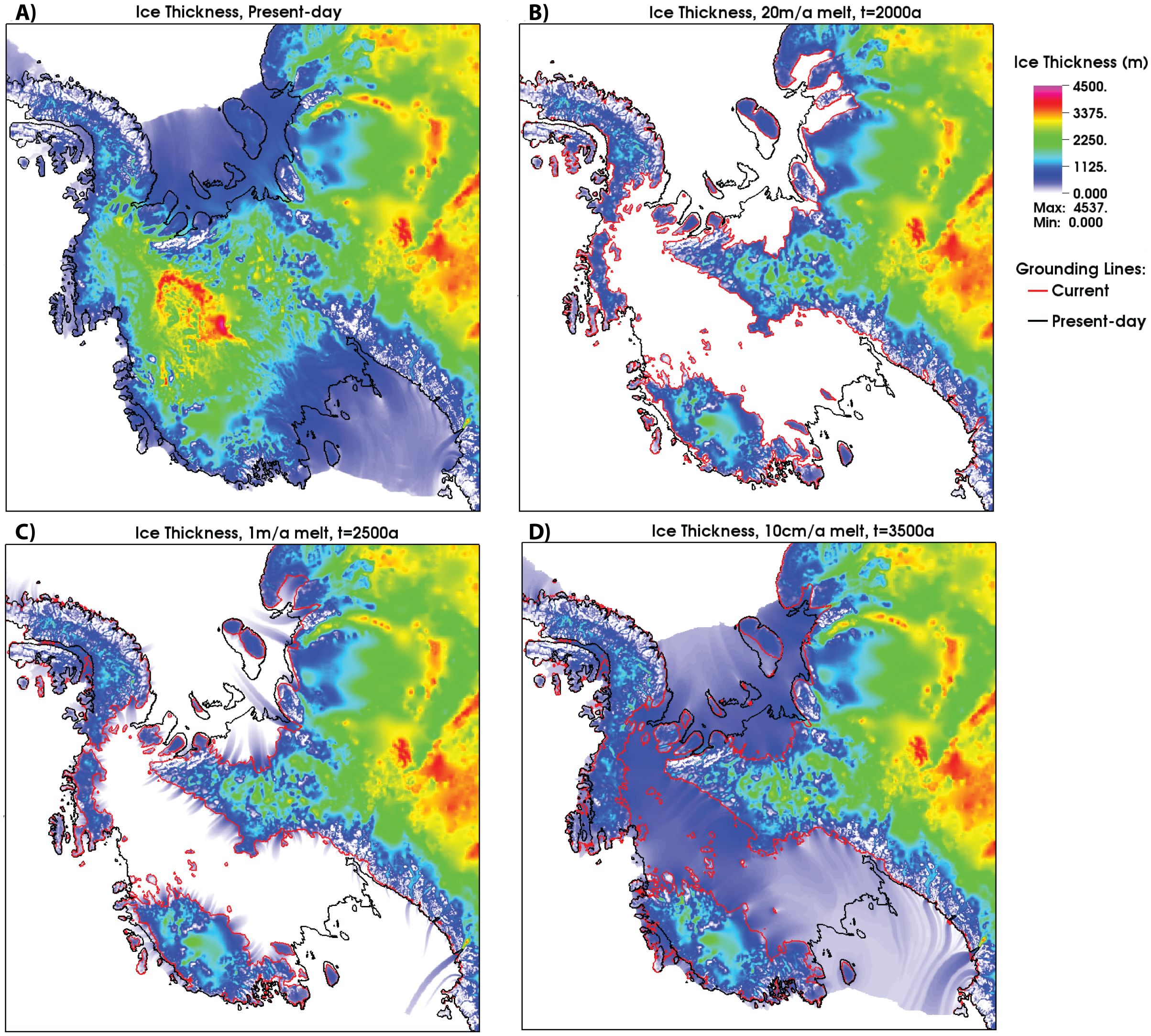

Figure 2.5: A) Modern ice thickness and final ice thickness for each subshelf melt rate experiment: B) 20 m/a after 1000 model years, C) 1 m/a after 1500 model years, and D) 10 cm/a after 1500 model years. The red line shows the simulated grounding line in each case and the black line is the modern day grounding line. The grounding line position for each experiment is similar. The 10 cm/a melt rate experiment is the only one that shows widespread thickening of the ice shelf over the WAIS basin, though thickening from flow convergence is evident in localized areas of the 1 m/a melt experiment.

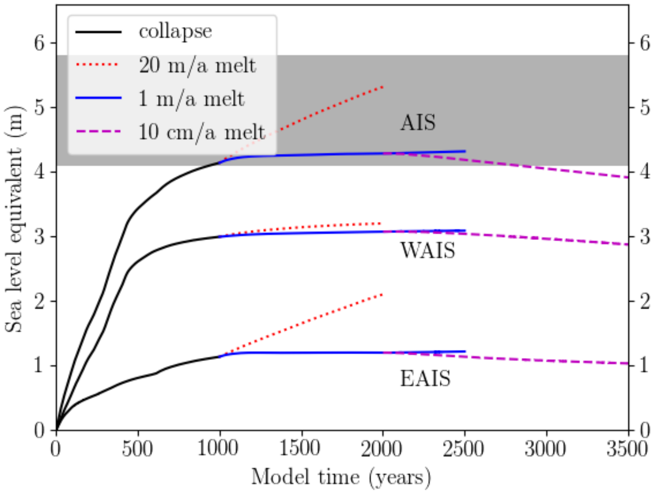

Figure 2.6: Sea level rise equivalent contribution due to ice sheet mass loss during each subshelf melt rate experiment compared to modern sea level. The 1 m/a experiment (blue dashed line) is seen to stabilize at ∼4.4 m sea level rise equivalent, while sea level in the 20 m/a melt rate experiment (red dash-dotted line) continues to increase indefinitely past 5 m and the 10 cm/a experiment (magenta dotted line) shows sea level rise potential continuing to decrease to 4 m when the experiments end. The black line shows the evolution of the ice sheet from the modern (at time 0) to the lowered topography as in Cornford et al. (2016). The gray band corresponds to the estimated range of Antarctic contribution to Last Interglacial sea level (McKay et al., 2011).

Chapter 3

Bayesian estimation of englacial radar chronology in Central West Antarctica

Englacial radar reflectors in the central West Antarctic Ice Sheet contain information about past dynamics and ice properties. Due to significant data coverage in this area, these isochronous reflectors can be traced over large portions of the ice sheet, but assigning ages to the reflectors for the purpose of studying dynamics requires incorporation of chronological data from ice cores. To date reflectors in the Marie Byrd Land region, we consider the Byrd ice core, strategically located between the catchments of Thwaites Glacier and the Siple Coast ice streams. We determine ages with uncertainty for four englacial radar reflectors spanning the ice thickness using Bayesian approaches to combine radar observations, an existing Byrd ice core chronology, and a simplified ice flow model. This method returns the marginal probability distribution of depth and age for each of the observed radar reflectors. The results also include inferences of accumulation rate at the Byrd ice core site during the last 50 ka that show a minimum accumulation rate during the Last Glacial Maximum at half the modern rate. The deepest continuous radar reflector is 25.67 ± 1.45 ka, less than 30% of the estimated age of the oldest ice at the Byrd ice core site despite being located at 70% of the ice depth, limiting the age of radar-interpretable ice in this region. The inferred reflector age profiles at the Byrd ice core site derived here compare favorably with the more recent WAIS Divide ice core record. However, uncertainty in reflector depth due to radar range precision contributes considerably to uncertainty in reflector age in a way that is not readily reducible using currently available ice-penetrating radar systems.

3.1 Introduction

Isochronous, englacial radar reflectors observed by ice-penetrating radar record the depth and extent of isosurfaces with shared physical properties (Siegert et al., 1998; Dowdeswell and Evans, 2004). These reflectors can map the age structure of an ice sheet, with the thickness of layers bounded by reflectors revealing information about ice flow dynamics and variable ice properties. Such observations have been used in Greenland and Antarctica to infer the ice flow history of the ice sheets in response to changing climate regimes in the past (MacGregor et al., 2015). To provide such historical climatic context, reflectors are assigned ages by correlation to a known chronology, such as at an ice core site (Cavitte et al., 2016). Dating englacial reflectors enables information from the entire ice volume, not only surface observations, to constrain ice sheet dynamics. However, combining information from ice cores and radar observations is intrinsically complicated by the fact that ice core chronologies assign discrete ages to samples of ice, while radar reflectors track packets of ice with finite thickness that span a range of ages, particularly at depth where age is more sensitive to depth due to shear thinning of the ice.

To understand how well radar reflectors can be dated, we use Bayesian methods to synthesize information from ice cores, radar sampling, ice flow modeling, and our knowledge of the leading sources of uncertainty within the radar and ice core data sources. We apply our approach to the central West Antarctic Ice Sheet (WAIS), an area containing the potential for unforced retreat where ice dynamics are of particular interest for projections of future sea level rise. In addition to being of scientific importance, the central WAIS is an area with concentrated radar surveys and two deep ice cores, the Byrd ice core (Gow et al., 1968) and the WAIS Divide ice core (Buizert et al., 2015). In particular, the proximity of the Byrd ice core (80.0167°S, 119.5167°W) to fast-changing ice of both the Siple and Amundsen Sea coasts in West Antarctica makes it a potentially important source of information about the response of the WAIS to climate change.

The Byrd ice core is co-located with several extensive radar surveys (Figure 3.1) and contains an ice record that extend back to more than 90 ka (Blunier and Brook, 2001), nearly back to the Last Interglacial. Rather than use existing chronologies for the age-depth relationship at the Byrd ice core, which do not sufficiently characterize its uncertainty, we generate our own chronologies using Bayesian strategies to synthesize an ice flow model with age-depth data obtained from volcanics sampled from the Byrd ice core (Gow et al., 1968; Gow, 1970; Hammer et al., 1997). This method allows us to simulate the co-dependence in dating errors within and between different radar reflectors.

The four reflectors in this study were chosen as a representative sample of the ice column and for their signal-to-noise ratio and continuity. It is possible to use this method to date additional englacial reflectors observed using radar in this area, but the usefulness of such ages extend only as far as the isochronous reflectors can be horizontally traced. While this method is less helpful for dating discontinuous reflectors, it could inform relative ages for sections of discontinuous reflectors adjacent to dated reflectors in the ice column (e.g. MacGregor et al., 2015).

We consider two quantities of interest in this problem: radar-inferred depths from observed two-way travel time (TWTT) and dated volcanics from the Byrd ice core. The primary sources of uncertainty in radar depths include the speed of electromagnetic radiation in ice, the density and thickness of the firn layer, and radar range precision. The error on range precision is determined independently for each reflector and the ice surface, while errors in velocity and firn are systematic (common) across all reflectors of interest in the ice column which are deeper than the firn layer. To estimate the ages of reflectors, we make use of dates determined for volcanic markers in the ice column (Hammer et al., 1997). In the absence of published uncertainty in the volcanic record, we use a Bayesian strategy to include an uncertain age uncertainty. An ice flow model is used to smoothly transfer information from the volcanics to the estimated depth of our reflectors of interest. To do so, it is necessary to infer flow physics parameters and accumulation rate history. Estimated ice flow and accumulation rate parameters are dependent on one another and on depth and are applied to the full ice column. A Bayesian framework allows us to describe all components of the problem within a single calculation, but requires stochastic sampling to estimate the marginal probability of reflector depth (and therefore age) as a function of observed TWTT and volcanics.

Section 3.2 discusses the formulation of the Bayesian problem and methods for finding solutions of the age and depth of observed englacial radar reflectors. Section 3.3 shows results for the probability distributions of reflector age and depth as well as a comparison to the WAIS Divide ice core chronology as an independent check on our results. We also calculate an error budget to determine the dominant contributions to age-depth uncertainty, discussed in Section 3.4.

3.2 Posterior distribution of englacial reflector age-depth

In order to assign ages to observed radar reflectors, we are interested in combining information from radar, ice flow physics, and dates from ice core volcanics at the Byrd ice core site. To do so, we take advantage of the versatility of a Bayesian approach to assemble the desired solution from a set of inter-related components. Our method preserves the chronological superposition of the ice column and correlation of errors with depth, estimates the probability of ice flow parameter values, and estimates a marginal probability of the age-depth profile.

The Bayesian formulation of the posterior probability distribution of radar reflector age is:

$$\begin{aligned} PPD(A_r) = \\ & PPD(D_r, \vec{f}, v_{ice}, S | TWTT_r, A_{IC}, D_{IC}) \propto \\ & \quad p(TWTT_r | D_r, v_{ice}) \cdot p(A_{IC}, D_{IC} | \vec{f}, S) \\ & \quad \cdot p(D_r) \cdot p(\vec{f}) \cdot p(S) \cdot p(v_{ice}) \end{aligned} \tag{3.1}$$

Computing the posterior probability distribution of reflector ages, $PPD(A_r)$

in Equation 3.1, requires jointly estimating the depths of the englacial reflectors of interest (D_r), ice flow model parameters and accumulation rate history ($\vec{f}$), radar velocity in ice (v_{ice}), and precision of the Byrd ice core chronology (S). We estimate these values given information about observed radar reflector two-way travel time ($TWTT_r$) and the ages and depths of volcanics (A_{IC}, D_{IC}) interpreted from the Byrd ice core record (Hammer et al., 1997).

We use priors, the rightmost four terms in Equation 3.1, to put physical bounds on sources of uncertainty as described in the following sections. Priors on D_r also preserve stratigraphic dependence of radar reflectors, requiring deeper reflectors be older than shallower reflectors. Likelihood functions, the first two terms on the right-hand side of Equation 3.1, evaluate if ice flow and radar model estimates are consistent with observations. The age likelihood (second term on right hand side of Equation 3.1) tests whether sampled ice flow parameters and accumulation rate history ($\vec{f}$) generate age-depth profiles consistent with the volcanic ages and depths (A_{IC}, D_{IC}). The scatter between modeled and observed ages determines precision (S) and whether estimates of D_r and v_{ice} are rejected or accepted relative to previously accepted solutions. The TWTT likelihood (first term on right hand side of Equation 3.1) tests agreement between observed two-way travel time ($TWTT_r$) and modeled TWTT using reflector depths (D_r) and v_{ice}. Both likelihood tests are used to accept or reject various “steps" through this solution space, resulting in an ensemble of accepted solutions. The elements of Equation 3.1 are discussed more thoroughly in subsequent sections.

3.2.1 Ice flow model at the Byrd ice core

Due to the inherent stratigraphic dependence of age in the ice column and the nonlinear effect of ice deformation on layer depths, we use a flow model to simulate the age-depth relationship. We use a simple, one-dimensional model of ice flow (Equation 3.2) which derives ice age from accumulation and strain rate, assuming constant horizontal strain rate in the upper part of the ice sheet and a shear layer of thickness h at the base of the ice sheet (Schwander et al., 2001). In the shear layer, the strain rate is assumed to decrease linearly and the bottom of the ice is assumed to slide with velocity $q \cdot v_0$, where v_0 is the horizontal velocity at the surface. The age of ice as a function of elevation from the bedrock interface is therefore:

$$A(z) = \int_z^H \frac{dz}{\epsilon_z \cdot \dot{a}(z)} \tag{3.2}$$

where strain is described by

$$\epsilon_z = \begin{cases} 1 - k(H - z), & h \leq z \leq H \quad (upper) \\ kz(q + \frac{1-q}{2h}z), & 0 \leq z < h \quad (lower) \end{cases},$$

and k is a constant such that $k = \frac{2}{2H - h(1-q)}$. H is ice thickness, which has been observed to be 2164 m at the Byrd ice core site (Gow et al., 1968) and z is the height above the bed. We invert for the remaining parameters: h, the depth to the Dansgaard-Johnsen shear layer (Dansgaard and Johnsen, 1969); $\dot{a}$, the time-dependent accumulation rate; and q, the ratio of horizontal velocity at the surface to that at the bed of the ice sheet.

The ice flow model accounts for two primary factors in the age-depth profile: burial as a function of accumulation rate, $\dot{a}$, and thinning as a function of strain, ϵ_z. In the simplest realization, ice deposited at a given time at the ice sheet surface will be found at a depth corresponding to the amount of subsequent accumulation. However, due to strain thinning at depth, ice of a given age will be less deep than would be expected if accumulation alone is considered.

The priors used for the ice flow parameters are defined by:

$$p(\vec{f}) = \begin{cases} p(h) \sim U[0, 0.5] \\ p(q) \sim U[0, 1] \\ p(\dot{a}_{i,i=1\ldots10}) \sim U[0.05, 0.25]\, m/a \end{cases} \tag{3.3}$$

The prior distributions of flow parameters and accumulation rate history, together denoted as $p(\vec{f})$, assume the shear layer is in the bottom half of the ice sheet depth (Cuffey and Paterson, 2010) and that ice at the bed of the ice sheet is moving no faster than the surface, which would allow for cases of both plug and creep flow. Accumulation rate as a function of depth, $\dot{a}$, is estimated for 10 distinct depth bins spanning the ice thickness at 200 m intervals. This allows for variability of accumulation rate over time.

3.2.2 Radar depth and error model

Radar pulses transmitted into the ice sheet reflect off surfaces of dielectric contrast in the ice that are the result of variations in ice fabric, composition, temperature, and rheology of ice (Fujita et al., 2000). The reflected signal is received by the radar system and recorded as two-way travel time (TWTT) from transmission to receipt. The reflector data in this analysis (Figure 3.2) were collected by the University of Texas Institute for Geophysics, including GIMBLE (Young et al., 2017), AGASEA (Holt et al., 2006), CASERTZ (Morse et al., 2002), and SOAR/WMB (Luyendyk et al., 2003) (Figure 3.1). Data used to trace reflectors between Byrd ice core and WAIS Divide ice core were collected from a DC-3 or Twin Otter airborne platform and used the HiCaRS2 coherent radar system with 60 MHz center frequency and 15 MHz bandwidth (Young et al., 2016).

In this study, we consider TWTT of four reflectors spanning the ice thickness in the region of central West Antarctica (Figure 3.2). These reflectors have been tracked using Halliburton's Landmark seismic interpretation software and can be tied to both the Byrd and WAIS Divide ice cores for dating using observations from the HiCARS system (Figure 3.1).

To estimate reflector depths from TWTT ($TWTT_{m,r}(D_r)$), we use a simple relation between the different velocities of the radar signal in air and in ice and incorporate several known sources of uncertainty, including: 1) variations in the radar velocity in ice due to ice temperature and fabric (v_{ice}), 2) vertical precision limitations of radar range detection (σ_{prec}), and 3) uncertainty in the firn correction (ϵ_{firn}) due to measurement errors in the ice density profile:

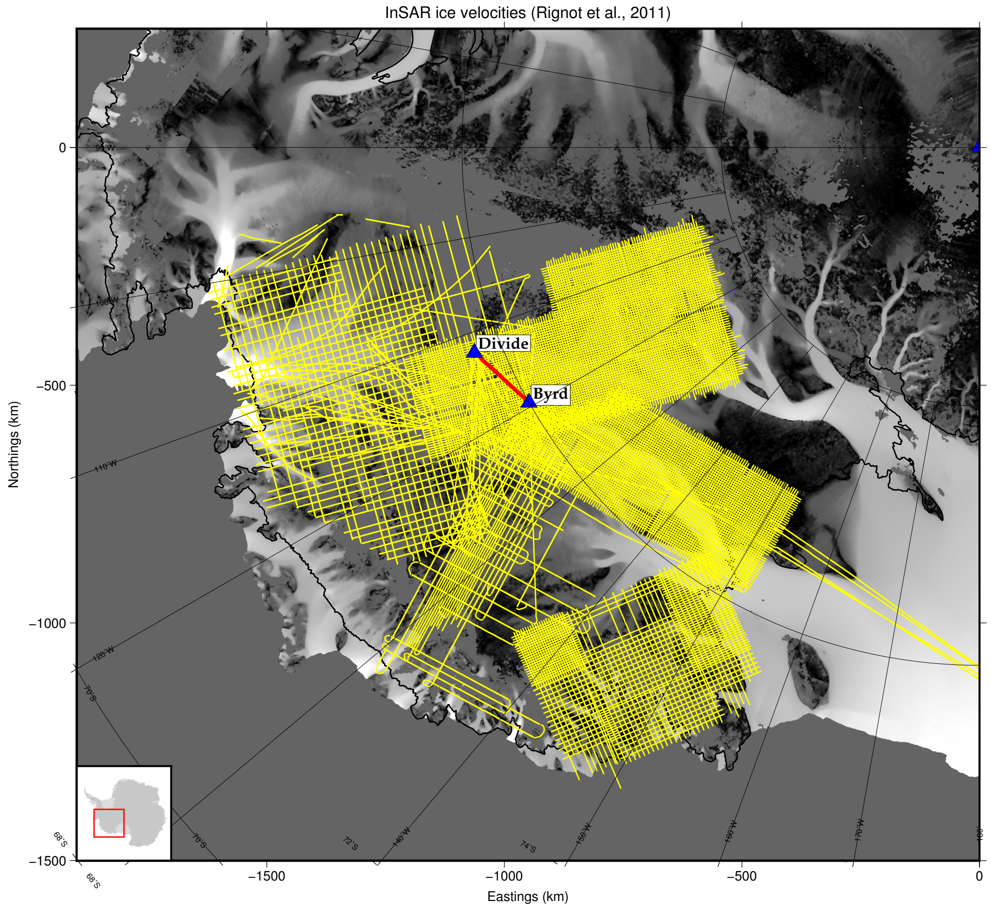

Figure 3.1: Map of central West Antarctic with available airborne geophysical radar surveys (yellow lines) and WAIS Divide and Byrd ice core locations (blue triangles) overlain. Gray shading is surface velocity (Rignot et al., 2011). The red line denotes the flight line along which the reflectors in this study were observed.

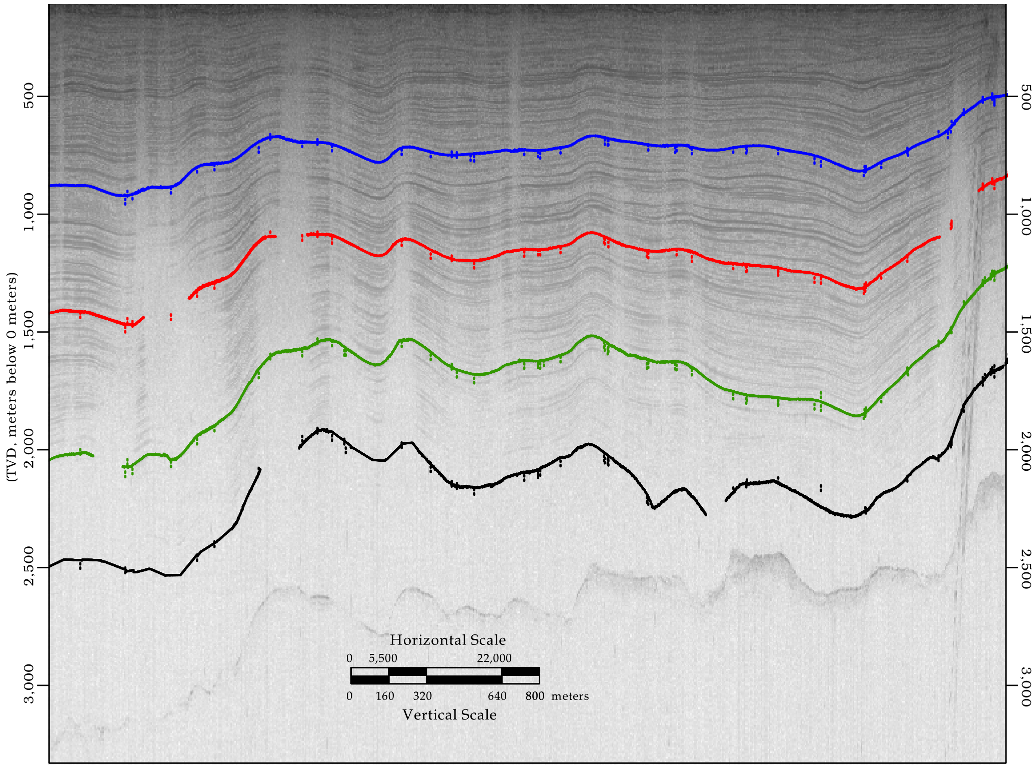

Figure 3.2: Radargram showing reflectors of interest near the Byrd ice core along flight line ICP6/MKB2l/F14T01a observed using the HiCARS2 radar system. Short vertical hatches along tracked reflectors show intersections with crosslines.

$$\begin{aligned} TWTT_{m,r}(D_r) + \sigma_{prec,r} = 2\frac{D_r - (d_{firn} + \epsilon_{firn})}{v_{ice}} \\ +(TWTT_{surf} + \epsilon_{prec,surf}) \end{aligned} \tag{3.4}$$

The complexity of local ice properties affecting the velocity at any location and depth make it difficult to know the true velocity. Empirical evidence suggests a range of expected velocities and we conservatively assume they are uniformly distributed such that: $p(v_{ice}) \sim U[168, 169.5]\, m/\mu s$ (Fujita et al., 2000). In lieu of detailed observations of ice properties with depth, we assume the value of v_{ice} is a constant throughout the ice column and apply it systematically to all reflector depths.

The radar pulse width determines vertical precision, $\sigma_{prec,r}$ (Millar, 1982). We assume a finite pulse width, meaning an infinitesimally thin layer of ice will appear in the survey to have a finite width. This can lead to errors in tracing isochronous reflectors, as the reflected energy from a finite depth will include ice with a range of ages. To account for this, we include uncertainty due to range precision, according to the signal to noise ratio of each reflector's radar amplitude as in Cavitte et al. (2016):

$$\sigma_{prec,r} = \frac{\Delta r}{\sqrt{SNR_r}} \tag{3.5}$$

The range resolution, Δr, is 8.4 m for all reflectors in the HiCARS2 system (Young et al., 2011). Values of the SNR for each reflector are shown in Table 3.1.

Finally, a firn layer with variable density (Gow, 1970) exists in the upper part of the ice sheet. The velocity of the radar is faster in firn than in solid ice. To correct for the underestimation of ice depth if the firn layer is not considered, we estimate the firn correction (d_{firn}), the difference between the ice thickness with and without the firn layer present . Errors in density, $\rho(z)$, are used to estimate the error in d_{firn}, ϵ_{firn}. These errors are known for the WAIS Divide measurements, but not for the Byrd ice core profile. In lieu of density measurement errors at the Byrd site, we assume the errors to be consistent with those observed at the WAIS Divide ice core. These errors are assumed gaussian, randomly sampled, and the firn correction is computed using the Dowdeswell and Evans (2004) relation:

$$d_{firn} = \frac{K}{n_i^{'}} \int (\rho_i - \rho(z))dz \tag{3.6}$$

where K is 0.85 m^3 Mg^{-1} (Robin et al., 1969), $n_i^{'}$ is the refractive index of ice ($n_i^{'}$=1.78), ρ_i is the density of ice (ρ_i=0.917 Mg m^{-3}) and $\rho(z)$ is the density of ice at depth z with units Mg m^{-3}.

The TWTT from the observing aircraft to the surface of the ice sheet is known from interpretation of the surface reflector, $TWTT_{surf}$. The computed depth of each reflector is relative to this surface reflector. Just as each reflector may have TWTT precision errors independent of the others, errors in the distance between the surface and the acquisition aircraft are common to all observed reflectors in the ice column. Therefore, a randomly sampled precision error, $\epsilon_{prec,surf}$, is applied systematically to all reflectors.

3.2.3 Metropolis Algorithm

At each iteration, a hybrid of Hastings and Gibbs sampling (Hastings, 1970; Gelfand et al., 1992) is used to select values for parameters of interest (those with priors in Equation 3.1). The algorithm accepts or rejects proposed sets of parameter values by comparison between the proposed and previously-accepted values, as measured by the likelihood. A high likelihood value represents good agreement between model and observations. According to the Hastings algorithm, if the likelihood associated with proposed parameters is higher than that of the previous accepted iteration, the proposed parameter values are accepted. Alternatively, lower likelihood values may be accepted with a probability determined by the change in likelihood.

There are two likelihood functions describing the model-data misfit in reflector depth and age, respectively:

$$\begin{aligned} p(TWTT_r|D_r,d_{firn},v_{ice}) &\propto \\ &exp[\frac{-\sum_{r=4}[TWTT_r - TWTT_{m,r}(D_r)]^2}{2\sigma^2_{TWTT}}] \end{aligned} \tag{3.7}$$

$$\begin{aligned} p(A_{IC}|D_{IC},\vec{f},S) &\propto \\ &exp[\frac{-S\sum_{j=61}[A_{IC,j} - A_{m,j}(\vec{f},D_{IC})]^2}{2\sigma^2_{A}} + R^6] \end{aligned} \tag{3.8}$$

Both likelihood functions must lead to acceptance in order for the proposed parameters to be accepted.

In the depth likelihood function, $TWTT_{m,r}(D_r)$ is based on the relationship between estimates of D_r and TWTT as in Equation 3.4. $TWTT_r$ is observed by ice-penetrating radar for each reflector, r. Uncertainty in TWTT, σ_{TWTT}, is taken to be the same as the radar range precision error which is a function of the signal-to-noise of each reflector amplitude and the bandwidth of the HiCARS radar system as described previously.

In the age likelihood function, the modeled age, A_m, is a function of ice flow model parameters and accumulation rate history, $\vec{f}$. A regularization term, R^6, is used to penalize large variability in the accumulation rates input to the ice flow model. R is a constant for each proposal equal to the ratio of the variance of the smoothed to unsmoothed proposed accumulation function. A_m comes from solutions to the forward ice flow model. We use $j = 61$ volcanic events from Hammer et al. (1997) as the observational target, A_{IC}, which do not include uncertainty information. These data represent dated volcanic deposits observed in the Byrd ice core and extend to $\sim$ 50 ka, though there is a lack of data in the brittle zone of the ice core between 300 and 900 m depth where the electrical conductivity cannot be measured (Hammer et al., 1997). Age uncertainty, σ_A, is nominally taken to be 1% of reflector age, a presumed underestimation of the true uncertainty. To determine additional uncertainty in volcanic age, we include a precision parameter, S, and use it to infer uncertainty in the volcanic record from scatter between our model and the observed data. In Bayesian nomenclature, S is a "nuisance" parameter that accounts for uncertainty in σ_A by using the sum of squared errors, E_m, as a measure of scatter between modeled age, A_m, and observed volcanic age, A_{IC}.

The posterior probability distribution of S is:

$$PPD(S) = Ga(\frac{k_e}{2} + \alpha, E_m + \beta) \tag{3.9}$$

where

$$E_m = \frac{\sum_j [A_{IC,j} - A_{m,j}(\vec{f}, D_{IC})]^2}{2\sigma_A^2} \tag{3.10}$$

Parameters α and β are assumed to be 1 as in the case for a non-informative gamma prior, $p(S) \sim Ga(\alpha, \beta)$. Unlike other parameters in our problem, values of S are selected through Gibbs sampling (Gelfand et al., 1992), effectively estimating reflector age uncertainty given the choice of ice flow model parameters and accumulation rate history for each iteration.

3.3 Dated englacial reflectors at the Byrd ice core

3.3.1 Reflector age and parameter estimates

The marginal probability distributions (1-D projections of the joint probability) of age and depth derived for englacial radar reflectors observed at the Byrd ice core site are shown in Figure 3.3 and Table 3.1. The age of the observed reflectors increases with depth, as expected due to stratigraphic burial of ice as it is deposited at the ice sheet surface. However, uncertainty in depth (and therefore age) does not increase monotonically with depth because of its dependence on reflector signal to noise ratio (SNR), as discussed in the next section. We estimate the oldest continuous radar reflector in central West Antarctica to be 24.9 ± 0.3 ka despite being observed at only 68% of the ice column depth (1466 ± 5 m). While this

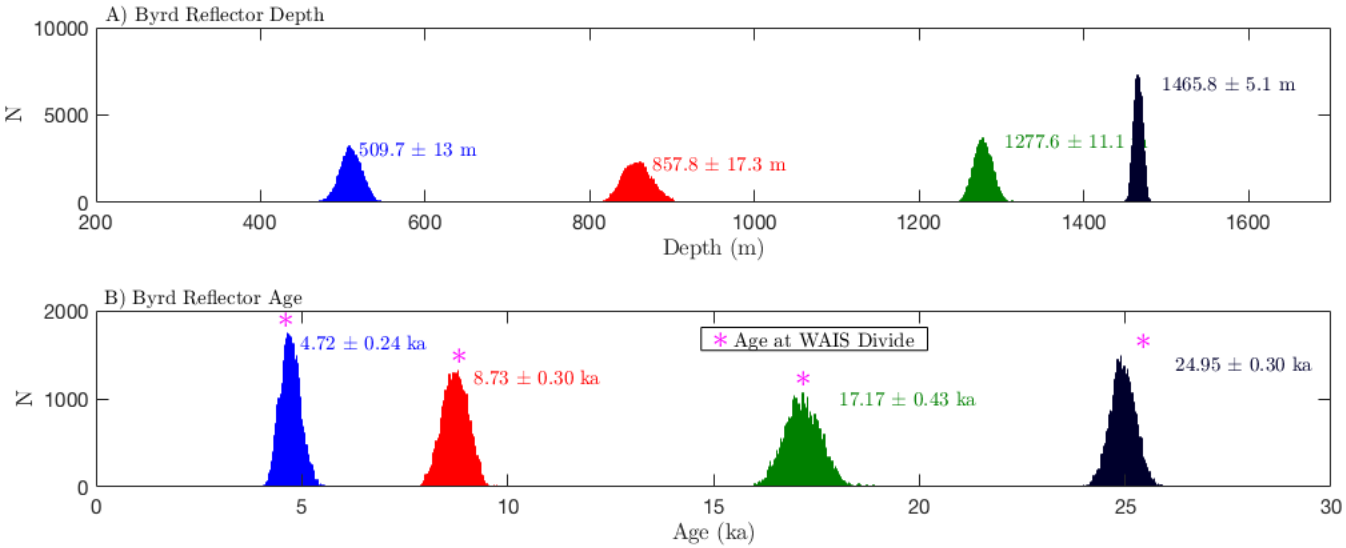

Figure 3.3: Posterior probability distributions of depth (top) and age (bottom) of 4 radar reflectors at the Byrd ice core. The width of the age and depth histograms for the Byrd ice core chronology represent uncertainty estimated by the methods used here.

constrains the age of ice near the bed of the ice sheet, it also limits the ability to use radar observations in this area to directly study ice sheet dynamics before the Last Glacial Maximum. Reflector 3, the second deepest reflector, is dated to 17.2 ± 0.4 ka which is consistent with the estimated age of the “Old Faithful" reflector, believed to be a relict from a series of volcanic eruptions. Reflectors 1 and 2 sample the ice column during the last 10 ka.

As has been established in previous work (Siegert et al., 1998; Dowdeswell and Evans, 2004), we assume radar reflectors are isochronous such that their age is the same whether observed at the Byrd ice core or the WAIS Divide ice core.

To compare between the two ice cores, we use Halliburton's Landmark seismic interpretation software to track radar reflectors through central WAIS via an existing radar survey flight line (Figure 3.1). The age-depth profiles at the Byrd ice core site (this study) and the WAIS Divide ice core effort (Buizert et al., 2015) are shown in Figure 3.4. Mean estimated age for each reflector at the Byrd ice core site compares favorably to that computed at the WAIS Divide ice core site (Figure 3.4).

In addition to computing the age and depth of radar reflectors, our method includes inversion for a number of parameters related to ice flow and paleo accumulation rates (Table 3.2) . Posterior probability distributions for these parameters are shown in Figure 3.6. Estimates of accumulation rate are uncertain, particularly in the brittle zone of the Byrd ice core (300 m to 900 m) where volcanic data are not available and corresponding posterior distributions look most non-gaussian. The widest, most uncertain accumulation rate posterior distribution represents depths below the deepest volcanic records ($\sim$1850 m), where there is limited constraint on the estimate. Even with these limitations, the general pattern of estimated accumulation rate reflects an expected pattern of lower accumulation rate during the Last Glacial Maximum ($\sim$1500 m), where we infer accumulation rates about half that of the modern (Figure 3.5).

Posterior probability distributions for other ice flow parameters estimated by the model are also shown in Figure 3.6. The ratio of surface to bed velocity, q, is inferred to be 0.9 ± 0.08 (where a ratio of 1 would indicate plug flow) indicating near plug flow at the Byrd ice core, which is consistent with the presence of liquid water at the ice sheet base found during drilling. The transition depth, h, is not

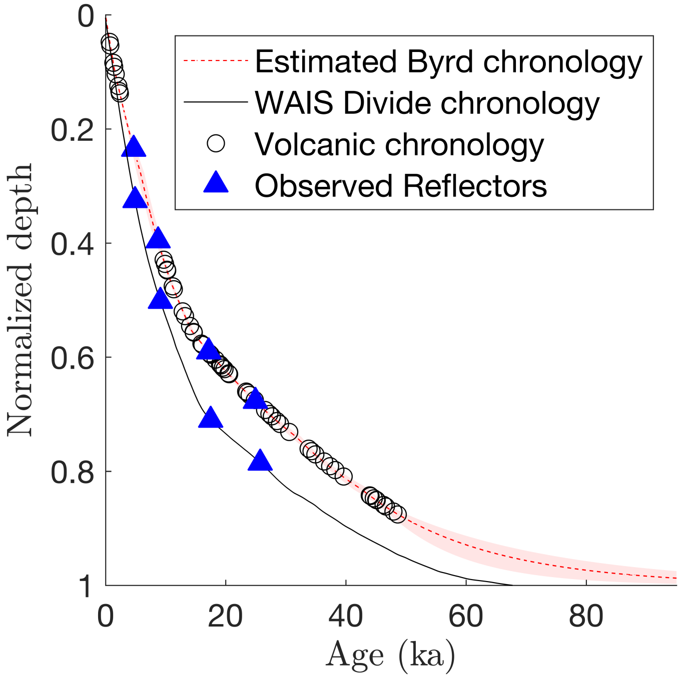

Figure 3.4: Modeled age-depth relationship with uncertainty compared to measured volcanic chronology from Hammer et al. (1997) (open circles). The WAIS Divide ice core chronology (Buizert et al., 2015) as a black line. Blue triangles show the age-depth of 4 radar reflectors at each of the Byrd and WAIS Divide ice cores; these reflectors are assumed isochronous and so expected to be the same age at either ice core.

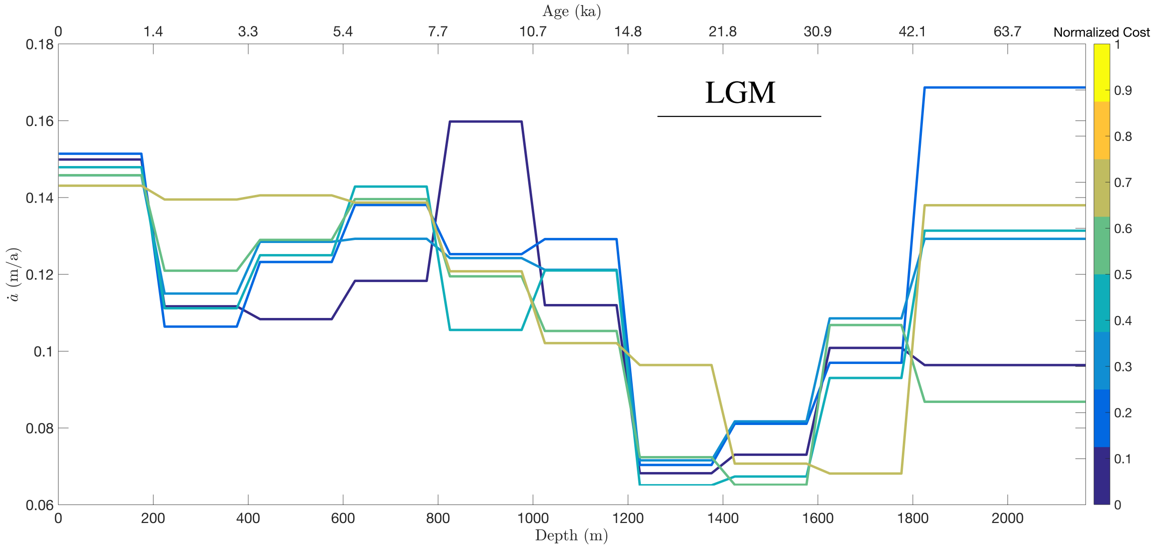

Figure 3.5: Accumulation rate as a function of ice depth colored by cost value which reflects each solution's fit to data. (Accumulation rate functions associated with lower cost are expected to be better solutions.) Accumulation rate is estimated in 10 depth bins at ∼200 m depth intervals. The Last Glacial Maximum (LGM) is indicated between 16 ka and 31 ka. Transitions between these intervals have been smoothed in this figure for ease of viewing.

well constrained by our estimates, likely because of the near-plug-flow conditions inferred by our model. We estimate the mean radar velocity through ice, v_{ice}, to be 168.4 $m/\mu s$ which is in the middle the range suggested by empirical estimates, but our posterior probablity distribution shows secondary peaks. Estimates of the precision parameter S imply 2.5% uncertainty in reflector age with a 95% confidence interval of [1.8%, 4.11%] (from $S \sim \frac{1}{\sigma^2}$), consistent with values that have been reported in ice core chronologies.

3.3.2 Error budget

To evaluate how much errors in each parameter contribute to uncertainties in age and depth of radar reflectors, we consider how uncertainty in reflector age and depth change when each parameter is assumed to be known with no error. To do so, we hold each model parameter fixed at its optimal value (Figure 3.3). If there is no change in the distribution of reflector age and depth, error in that model parameter has no influence on the result.

We find errors in depth contribute 25%, 37%, 77%, and 43% to uncertainty in depth to reflectors 1, 2, 3, and 4, respectively. This suggests that deeper in the ice column an increasing portion of uncertainty in age is from errors in reflector depth. However, high reflector SNR (and therefore radar range precision) can mitigate this effect. As seen in Figure 3.3, the deepest observed reflector, which may be expected to have the largest depth uncertainty, instead has relatively high SNR and therefore low uncertainty.

Uncertainty in age is also sensitive to the accumulation rate profile which

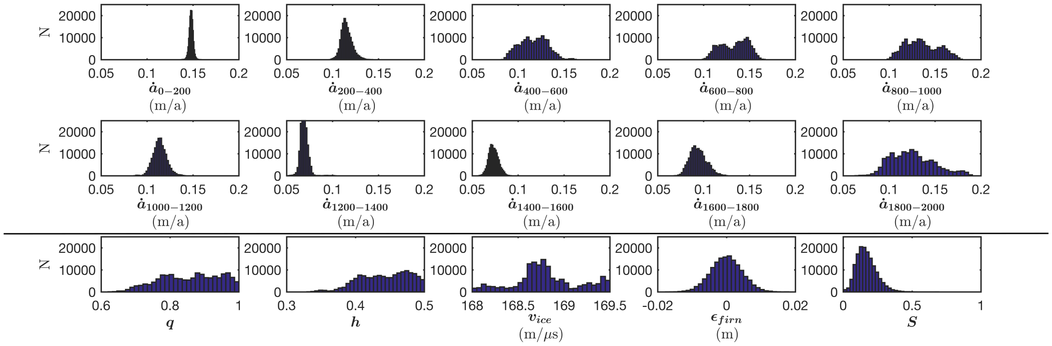

Figure 3.6: Posterior probability distributions of inverted parameters, including accumulation rate, q, h, v_{ice}, ϵ_{firn}, and S. Accumulation rate paramter values are assigned to 200 m depth intervals indicated by the subscript. While a few parameter distributions appear non-gaussian, parameter values are well sampled and generally single-peaked. The precision parameter, S, has an expected gamma distribution and ϵ_{firn} is normally distributed, as expected.

accounts for up to 40% of the age uncertainty of each reflector. Accumulation rates in localized portions of the ice column do not individually influence the age uncertainty as much as the full accumulation rate profile, but rates in the upper part of the ice column have more impact due to their influence on the age of ice below. Other individual ice flow parameters play a far smaller role in the error budget.

3.4 Discussion

For this study, we employ a simple Dansgaard-Johnsen-type ice flow model (Schwander et al., 2001). We do not include a separate term for basal melting, which is likely occurring or has occurred at this site as liquid water was observed at the bed during drilling (Gow et al., 1968). The inclusion of a melt condition is expected to increase accumulation rate estimates to account for ice loss at the bedrock interface. We exclude basal melting because we lack estimates of basal melt rate over time. However, this method could be adapted to incorporate a more sophisticated flow model with additional parameters such as a non-zero melt rate.

To estimate the ice flow and accumulation rate parameters in our model, we must assume the effective number of degrees of freedom, k_e, because it is not known. The number of degrees of freedom helps determine the significance of errors between our model and the volcanic chronology. Because we use these errors as a measure of uncertainty through parameter S, k_e has a direct role in determining the uncertainty in age estimates. Estimates of k_e using our ice flow model to represent the effect of uncertainties in ice flow parameters and accumulation rates on age estimates varied depending on assumptions about these model parameters. Given this variation and the potentially circular logic in this method, we instead choose $k_e = \frac{j}{2}$ = 30.5, which assumes there are strong correlations among age solutions. This is reasonable because we expect errors in age and depth are related within the ice column. As shown in Figure 3.4, this choice does not affect mean estimates of reflector age and depth, but it does have some affect on the uncertainty associated with them.

Uncertainties in our estimates of radar reflector depth are significant compared to those derived from the age determination alone. These relatively large uncertainties from the radar can be attributed to radar range precision in the determination of reflector depths. This precision is a function of the signal-to-noise

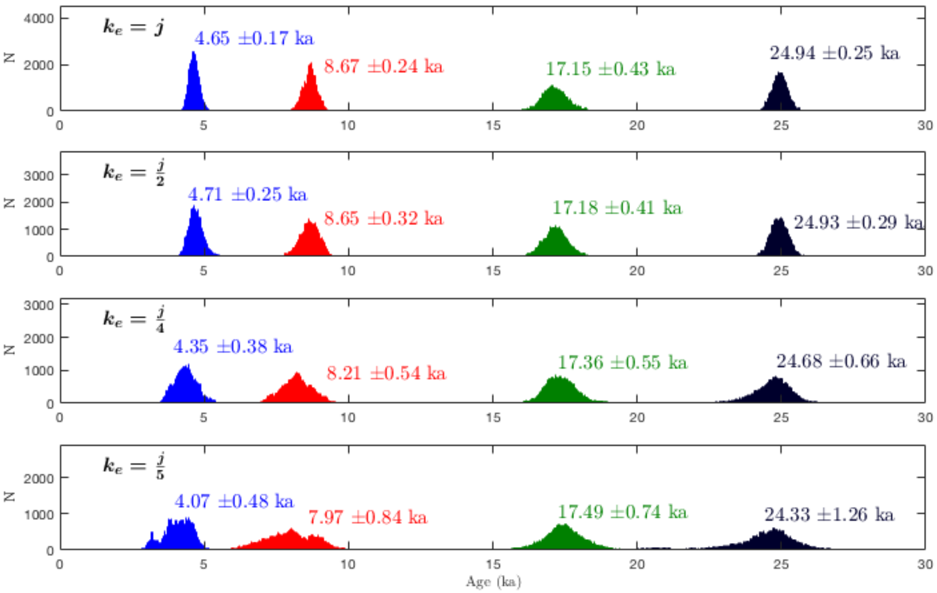

Figure 3.7: Comparison of reflector age for different degrees of freedom, k_e, relative to the number of volcanic data points, $j = 61$. The choice of k_e has an effect on uncertainty in reflector age estimates, but does not greatly impact mean estimates.

ratio (SNR) of the radar reflection and bandwidth of the radar system used to obtain the reflections (Cavitte et al., 2016). Increasing SNR would improve range precision and reduce uncertainty, however our method already selects for high SNR in analyzing only the brightest reflectors in the ice column. As a result, we expect the data do not support improving precision in this way. Increasing bandwidth (15 MHz for the HiCARS radar system) would also improve the radar range precision, however this is technically challenging for modern airborne radar systems because antenna tuning is difficult for bandwidths greater than 25% of the center frequency (60 MHz for the HiCARS system). Ground penetrating radar systems can have higher bandwidth, but are more limited in their spatial coverage. Further, while higher resolution can be obtained by increasing bandwidth and center frequency, penetration through the ice declines and reflections become increasingly discontinuous with increasing bandwidth (Cavitte et al., 2016).

3.5 Conclusion

We derive ages for isochronous radar reflectors observed near the Byrd ice core which include estimates of uncertainty in ice flow parameters and accumulation rates in the region of Marie Byrd Land, West Antarctica. Such radar observations may reveal englacial stratigraphy indicative of past ice flow, but require dating to put constraints on interpretations of ice dynamics. The Byrd ice core location connects WAIS Divide to the ice streams of the Siple Coast and the Marie Byrd Land icecap via radar observations and this work contributes to constraining uncertainty in the chronology of englacial radar reflectors.

Table 3.1: Depth and age mean and standard deviation for four radar reflectors near Byrd Station, West Antarctica used in this study. The radar-observed two-way travel time (TWTT) to each reflector and its associated signal-to-noise ratio (SNR) used to compute TWTT uncertainty is also shown.

Reflector	TWTT (μs)	Depth (m)		Age (a)		SNR (dB)
		μ	σ	μ	σ	
1	8.44	510.1	13.1	4711	246	10.41
2	12.54	854.6	18.0	8653	318	8.13
3	17.55	1277.9	10.8	17177	413	11.63
4	22.42	1460.0	5.2	24928	286	21.22

Our estimates of the reflector age-depth are consistent with independent comparison to the same reflectors dated using the WAIS Divide ice core chronology (Buizert et al., 2015), although large uncertainties due to radar range precision preclude a strong test of inferences between the two cores. Our results indicate the oldest continuous radar reflector datable using existing ice cores and radar surveys in central West Antarctica is located at ~70% ice depth at the Byrd ice core site and dates to ~ 24.9 ± 0.3 ka. The same reflector is observed at ~80% ice depth in the WAIS Divide ice core. While the Byrd ice core has been dated to as old as ~ 94 ka at its base (Blunier and Brook, 2001), continuous radar reflectors do not extend deep enough in this region to leverage the ice core to date older radar-observed ice in the central WAIS. The range precision of existing ice-penetrating radar systems is the biggest contributor to uncertainty in radar reflector age. This uncertainty is largely irreducible due to practical trade-offs in airborne system design and leads to potentially significant uncertainty in reflector age at depth.

Table 3.2: Mean and standard deviation of parameter values estimated in this study and used to estimate reflector age and depth.

Parameter	Median $\pm$ 1σ	Parameter	Median $\pm$ 1σ
$\dot{a}$(d $<$ 200 m)	14.8 $\pm$ 0.2 cm	q	0.9 $\pm$ 0.08
$\dot{a}$(200 m $\geq$ d $<$ 400 m)	11.4 $\pm$ 0.6 cm	h	0.45 $\pm$ 0.03
$\dot{a}$(400 m $\geq$ d $<$ 600 m)	11.1 $\pm$ 1.4 cm	v_{ice}	1.674 $\times10^8$ $\pm$ 3.227 $\times$ 10^5 m/s
$\dot{a}$(600 m $\geq$ d $<$ 800 m)	14.2 $\pm$ 1.2 cm	S	0.154 $\pm$ 0.07
$\dot{a}$(800 m $\geq$ d $<$ 1000 m)	13.0 $\pm$ 1.8 cm		
$\dot{a}$(1000 m $\geq$ d $<$ 1200 m)	11.2 $\pm$ 0.7 cm		
$\dot{a}$(1200 m $\geq$ d $<$ 1400 m)	6.8 $\pm$ 0.3 cm		
$\dot{a}$(1400 m $\geq$ d $<$ 1600 m)	7.2 $\pm$ 0.5 cm		
$\dot{a}$(1600 m $\geq$ d $<$ 1800 m)	9.2 $\pm$ 1.0 cm		
$\dot{a}$(1800 m $\geq$ d)	11.6 $\pm$ 2.5 cm		

Chapter 4

Model-Data Comparison of Englacial Isochrones

Airborne ice-penetrating radar surveys covering central West Antarctica provide englacial information pertaining to ice flow and subglacial boundary conditions. Internal ice layers have been dated and tracked for hundreds of kilometers in this region by the authors, giving a broad testbed for studying paleo ice sheet conditions. Ice sheet models can also be used to test hypotheses related to ice flow and boundary conditions, but have not thus far been used to simulate englacial surfaces on a regional scale for comparison to observations.

The geometry and distribution of englacial isochrones reveal information about the flow history and boundary conditions acting on the ice sheet over time. We demonstrate a method for deriving englacial isochronous surfaces from the Ymir ice sheet model velocity fields using $Paraview$. Streamlines are computed according to advection of particles through a simulated 3D velocity field and the result is used to interpolate surfaces of constant age. Ice-penetrating radar observations of englacial isochrones are also interpolated into surfaces and are compared to the simulations.

Due to model limitations, the results included in this analysis are preliminary, but demonstrate the effectiveness of deriving simulated englacial surfaces from the Ymir ice sheet model. We expect model-data differences will result from both uncertainty in model boundary conditions and deformation due to ice flow history. To separate this effect, we perform three experiments varying basal topography and geothermal flux to investigate the sensitivity of surface geometry to these changes.

4.1 Introduction

The geometry of englacial radar reflectors encode information about both local basal properties and past ice dynamics. The central West Antarctic Ice Sheet (WAIS) is one area of hypothesized instability where evidence of past retreat may be preserved in the deformation of englacial reflectors observed in the modern ice sheet. However, there are many processes which can influence the shape of observed reflection surfaces (Siegert et al., 2004), including both boundary conditions and ice dynamics. To isolate the signature of dynamic processes such as flow redirection during grounding line retreat into the WAIS subglacial basin, it is necessary to identify the effects of boundary conditions on engacial isochrone geometry.

Analyzing the role of boundary conditions on shaping englacial reflectors can be achieved using ice sheet model sensitivity experiments. Aspects of these processes have been explored in 1D (Parrenin et al., 2017), 2D (Parizek et al., 2013), and simple 3D (Leysinger Vieli et al., 2007) ice sheet models, but higher-order 3D models are more suitable for simulating the complexities of spatially-extensive englacial surfaces and for direct comparison to observations of englacial isochrones. Further, sophisticated thermomechanical coupling is required to incorporate realistic ice viscosity and subglacial ice fluxes which can affect ice flow and the subsequent shape of englacial isochrones.

While there are a number of higher-order ice sheet models available (e.g. Larour et al., 2012; Winkelmann et al., 2011), we use the relatively recent Ymir ice sheet model (Isaac et al., 2015) because its adjoint-based solvers are efficient for solving the thermomechanically-coupled 3D Full Stokes ice flow equations. The steady state model inverts for basal traction and computes a 3D velocity field consistent with observations of surface velocity, geometry, and accumulation rate. We use the resulting velocity field to derive simulated englacial isochrones toward the goal of testing the null hypothesis that the WAIS has been stable through time. Discrepancies between simulations of a steady state WAIS and observed englacial reflectors are expected to be indicative of dynamic instability. However, we first conduct experiments to determine how much of the model-data discrepancies could be due to uncertainty in model boundary conditions rather than ice dynamics.

We focus on evaluating the effects of two basal boundary conditions: basal topography and geothermal flux. These are expected to strongly influence englacial reflector geometry. Englacial reflectors deform to flow around, over, and through topographic obstacles, including mountains and trenches. Friction from small-scale roughness and pinning points from local topographic ridges can control ice velocity that may introduce features such as folds, drawdowns, and shear margins into englacial reflectors. Elevated heat flux, on the other hand, may contribute to a wet subglacial environment which reduces friction and promotes sliding. Subglacial melting in this process may manifest as drawdowns in englacial reflectors. In addition to community-standard datasets for these boundary conditions (Fretwell et al., 2012; Shapiro and Ritzwoller, 2004), we use higher-resolution estimates based on the latest observations (Young et al., 2017; Schroeder et al., 2014).

In the following sections, we describe the Ymir ice sheet model and our sensitivity experiment design as well as the available observations of englacial surfaces and boundary conditions (Section 4.2). We demonstrate our ability to derive simulated englacial isochrones in three dimensions and qualitatively compare preliminary model results to observations (Section 4.3). We then discuss further model development required to conclude the sensitivity analysis and produce final estimates of simulated isochrones (Section 4.4).

4.2 Methods

4.2.1 3D thermomechanical ice sheet modeling

The Ymir ice sheet model (Isaac et al., 2015), developed at the Institute for Computational and Engineering Sciences at the University of Texas, is a 3D Full Stokes model which uses an adjoint-based inversion to infer basal traction given basal topography as well as surface velocity, geometry, and accumulation. Additional functionality for thermocoupling has been added which allows for subglacial melting and appropriate thermal balances within the ice (Zhu et al., 2016). The model does not include a dynamic grounding line and is therefore best suited for steady state simulations such as those performed for this study. We configure the model with a mesh of 8 evenly-spaced vertical levels and use cells with a maximum horizontal-to-vertical aspect ratio of 300 (Figure 4.1). Previous versions of the model used as few as 2 vertical levels, which was not sufficient for this analysis. We use 8 levels here because it is the maximum vertical resolution currently achievable given memory limitations of the model as run on the Lonestar5 supercomputer at the Texas Advanced Computing Center. Lower aspect ratios are applied near more dynamic regions closer to the grounding line.

While the adjoint method is generally efficient for solving the Full Stokes equations, we find the vertical resolution necessary for our analysis results in long computational times and increased memory usage. Since publication of the model, development has sought to address these issues, but more work is needed. This topic is discussed further in Section 4.4.

4.2.2 Boundary conditions and experiment design

We explore the influence of model boundary conditions on simulated englacial geometry in the central West Antarctic region (Figure 4.2.1), which covers the fast-thinning Thwaites Glacier, variable ice streams along the Siple Coast, and the relatively stable WAIS Divide. For sensitivity analysis, we test the effects of changing between two estimates of basal topography and two estimates of geothermal flux (Figure 4.3). These boundary conditions represent established community standard datasets (Fretwell et al., 2012; Shapiro and Ritzwoller, 2004) as well as the latest high-resolution, observation-driven estimates of subglacial conditions in central West Antarctica (Young et al., 2017; Schroeder et al., 2014). These boundary conditions are paired to create three experiments for this preliminary analysis (Table 4.1). Including additional boundary condition experiments in future work would be straightforward.

The Bedmap2 boundary condition (Fretwell et al., 2012) is a product of a large consortium of researchers to combine various types of data into community datasets, including basal topography of Antarctica. UTIG-collected data was included in that effort at the time and Bedmap2 is still used generally as the community standard for modeling efforts. Since developing Bedmap2, UTIG has continued to collect additional data in the area, particularly in the Marie Byrd Land (MBL) region of Central West Antarctica (Young et al., 2017). The additional data has been included here in an updated bed topography field which we refer to as MBL+. The MBL+ dataset has the advantage of more detailed topography in the MBL region which reveals additional troughs along the Amundsen Sea Coast. It also more accurately constrains the extent of the MBL highlands where ice is shown to persist through major ice sheet retreat (Muldoon et al., 2018a, in review). The decreased extent of elevated topography may have implications for the pattern of retreat and the position of the resulting grounding line. These differences could result in changes in the geometry of surviving ice. An alternative basal topography developed at UTIG uses a statistical approach to approximate basal topography between radar flight lines (Goff et al., 2014). This dataset computes a realistic topography between flight lines, but is confined to the Thwaites Glacier catchment, so we do not include it in the initial set of experiments.

The two geothermal flux boundary conditions were derived independently.

The Shapiro and Ritzwoller (2004) geothermal flux is the best continent-scale estimate of geothermal flux available and is one of a few geothermal flux datasets often used in model boundary conditions.[1] The estimate was determined through similarity analysis with geothermal flux estimates elsewhere in the world and exhibits elevated geothermal flux over West Antarctica, which is underlain by a rift system. An independent estimate of geothermal flux by Schroeder et al. (2014) uses ice-penetrating radar estimates of bed specularity. High specularity is inferred to indicate the presence of subglacial meltwater as a result of elevated geothermal heating of the ice. This dataset reveals a heterogeneous distribution of geothermal flux, but is limited to the domain of the Thwaites Glacier Catchment. Outside this region, we assume the Shapiro and Ritzwoller (2004) estimate applies. As seen in Figure 4.3, the two complement each other, though Schroeder et al. (2014) do not find the same large hotspot in the Thwaites Glacier Catchment as Shapiro and Ritzwoller (2004). Additional geothermal flux estimates are available based on aeromagnetic data (Martos et al., 2017) and seismic modeling (Wiens et al., 2017). These datasets have yet to be reconciled with each other, so we exclude them from the initial set of experiments.

---

[1] The other continent-scale geothermal flux estimate sometimes used in modeling studies was computed by Maule et al. (2005) based on satellite magnetic data. However, this result generally does not match as well as Shapiro and Ritzwoller (2004) to available localized observations.

Experiment	Shorthand	Bed topography	Geothermal Flux
Bedmap2/Shapiro	BSR	Fretwell et al. (2012)	Shapiro and Ritzwoller (2004)
MBL+/Shapiro	MSR	Young et al. (2017)	Shapiro and Ritzwoller (2004)
Bedmap2/Schroeder	BSch	Fretwell et al. (2012)	Schroeder et al. (2014)

Table 4.1: Sets of boundary condition used in experiments in this analysis. Each combination consists of a basal topography and geothermal flux pair and may be referred to by their shorthand in the text.

4.2.3 Simulating englacial surfaces

For comparison to observed englacial isochrones, the 3D velocity field simulated by Ymir is post-processed into isochronous surfaces using the $Paraview$ data analysis and visualization software. This software is an open-source platform for scientific visualization which makes use of the Visualization Toolkit (VTK) for 3D computer graphics. $Paraview$ allows for interfacing with VTK through python scripts which allows for automated post-processing of our model output. The automation pipeline scripts are included as supplemental information and available online.

Ymir produces a field of 3D ice velocities in a mesh with 8 vertical layers and a horizontal quadrilateral mesh with horizontal refinement in areas of fast or converging ice flow. Tetrahedralization and tessellation are performed on the Ymir velocity field to improve the mesh for particle tracking and streamline continuity. Seed points are positioned on the ice surface at each mesh vertex to provide interpolation points for $Paraview$'s built-in advection scheme. Subdivision of the mesh is used to add additional seed points between vertices to increase the density of advected particles. *Paraview*'s Stream Tracer filter is used to compute streamlines from each surface seed point through the velocity vector field until they terminate at the edge of the domain. The integration time along each streamline represents the age of ice at any position along that streamline.

The streamline field is contoured by age to identify collections of isochronous points. These points are then interpolated into a surface using a cubic spline and masked to the model domain. This method can be used to derive an isochronous surface for any age, though a higher density of contour points results in a better interpolated surface. For each experiment, we have done this processing for the four isochrones for which we have observations.

4.2.4 Observed englacial surfaces

Reflectors observed by ice-penetrating radar are assumed to be isochronous and can be interpolated between survey flight lines to compute englacial isochronous surfaces. The extent of airborne ice-penetrating radar surveys conducted by the University of Texas Institute for Geophysics (UTIG) over the central WAIS is shown in Figure 4.4. Observations in this analysis were collected using airborne ice-penetrating radar from several surveys by UTIG, including GIMBLE (Young et al., 2012), AGASEA (Holt et al., 2006), CASERTZ (Morse et al., 2002), and SOAR/WMB (Luyendyk et al., 2003). Radar reflectors, resulting from dielectric contrasts in the ice, have been traced on radar cross sections using Halliburton's *Landmark* seismic interpretation software to map their depths. We consider the four reflectors dated in Muldoon et al. (2018b, in review) which have been extended as far as they were continuous. Depth information from these reflectors were then interpolated into isochronous surfaces using a cubic spline (Figure 4.5). Percent depths (Figures 4.8 – 4.11) are determined using ice thickness measured by the same ice-penetrating radar data.

4.3 Results

4.3.1 Simulation progress and model limitations

Current results are preliminary due to model resolution limitations. Three simulations with various boundary condition combinations (Table 4.1) have been performed as a proof of concept and initial analysis of the role of uncertain boundary conditions on englacial horizon geometry is included here. Sufficient vertical resolution, empirically determined to be more than 4 vertical layers, is needed to compute ice flow streamlines. However, none of the high-resolution experiments performed for this study reached convergence of the optimization algorithm in the maximum allotted supercomputing queue time (48 hours) for the Lonestar5 computer at the Texas Advanced Computing Center using the maximum 4104 cores. Special accommodations have been made to extend the simulations to 120 hours, but the results of this test are pending. In lieu of converged output, simulations in this analysis are compared after 6 iterations of the optimization algorithm, the minimum number achieved by all three experiments.

4.3.2 Horizontal surface velocity

Ymir inverts for a basal sliding condition given surface conditions including velocity and geometry. As such, it is expected the modeled surface velocity will match well to the given surface observations when the model reaches convergence. After 6 iterations of each run, we find the horizontal surface velocities have the same pattern as the Rignot et al. (2011) velocity field, primarily in the location of fast-flowing ice streams (Figure 4.6). In general, the Ymir output estimates higher velocities in the interior WAIS than Rignot et al. (2011), though the latter contains missing values along the slow-flowing ice divide. The Bedmap2/Shapiro result (Figure 4.6b) demonstrates the best match to the Rignot et al. (2011) velocity, which may be because that combination of boundary conditions contains the least detail. This experiment may therefore be more efficient to solve and so closer to convergence than the other experiments after 6 iterations. This explanation is consistent with the fact that the MBL+/Shapiro experiment, which has the highest resolution basal topography, matches Rignot et al. (2011) least well.[2]

Both runs using the Bedmap2 topography (Figures 4.6b and 4.6c) show an interesting discontinuity in the path of ice flowing toward the Siple Coast. This feature is missing from the more detailed MBL topography which may indicate additional resolution of the bed topography in this region reveals there is no obstacle.

---

[2] While the complexity of the geothermal flux field may also affect this efficiency factor, we note inclusion of the Schroeder et al. (2014) geothermal flux differs from the Shapiro and Ritzwoller (2004) boundary condition in only a small portion of the boundary condition domain. As a result, we expect this difference to have a much smaller effect.

However, it may also be the case that the MBL topography, with increased detail, is slower to converge than the other model runs and that feature may become apparent in later model iterations.

4.3.3 Vertical surface velocity

As discussed further in Section 4.4, the Ymir model currently struggles with correctly estimating the surface, and presumably englacial, vertical velocity. Increasing the vertical resolution, constraining estimates to be negative (into the ice), and instituting a stricter objective function with more weight on the surface vertical velocity has helped, but more work is needed to be confident in the model's approximation of vertical velocity, particularly at ice divides.

Figure 4.7 shows estimates of surface vertical velocity for the three experiments in this analysis. Vertical velocity at the ice sheet surface is akin to (negative) surface accumulation, so these estimates are compared to the Arthern et al. (2006) microwave-derived estimate of surface accumulation used as a model boundary condition. We find Ymir surface velocities are lower than Arthern et al. (2006) surface accumulation estimates except in areas of fast flowing ice where drawdown leads to larger vertical velocities in the model. Surface vertical velocities also largely do not recreate increased surface accumulation along the coast. We have not tested other surface accumulation boundary conditions in the model, though it is equipped to do so. However, we expect current biases in the vertical velocity field in this model version are numerical (not physical) and will need to be addressed with additional model development as discussed in Section 4.4.

4.3.4 Simulated englacial isochrones

Isochronous surfaces with four distinct ages spanning the ice thickness (5 ka, 9 ka, 17 ka, and 25 ka) were derived from the Ymir 3D velocity field as described above. We compare the geometry of these to the four observed isochrones identified in Muldoon et al. (2018b, in review). Figures 4.8 – 4.11 show the normalized depth to each of these simulated and observed surfaces. For all simulated surfaces, gaps in the surface (white areas) are indicative of where the englacial surface intersects the bed due to drawdown (white bordering yellow) or where ablation may be taking place (white bordering purple). However, as discussed below, care must be taken in this interpretation because the surfaces are largely dependent on the velocity field.

The youngest, shallowest isochrone (4.7 ka, Figure 4.8) is observed to have the largest surface as a result of the relative ease with which it could be tracked along survey flight lines. The depth of this surface is about ~ 0.25H of the ice thickness (H) with variations of 5-10% of H in the map-east portion of the domain. The surface dips below 50% of the ice depth as it enters the Thwaites Glacier Catchment, consistent with drawdown due to fast flow. The simulated surfaces show a similar pattern of drawdown in the Thwaites Glacier catchment, but demonstrate more extreme depths at either end of the scale. This is consistent with anomalously low estimates of vertical velocity at the ice sheet surface in the interior and anomalously high vertical velocities in the outlet glaciers. As a result, ice near the surface remains there until reaching an area of fast flow where it is quickly drawn down to greater depth.

The observed surface does not appear to exhibit the same inland-reaching influence of ice streams along the Siple Coast as the model surfaces demonstrate. This result may evolve with additional iterations of the model or may be consistent with the diffuse nature of velocities inland of the Siple Coast, particularly for the MBL+/Shapiro and Bedmap2/Schroeder experiments. Outside the observed surface domain, the experiment using MBL bed topography (Figure 4.8c) shows noticeable evidence of drawdown from the divide to the Marie Byrd Land coast, reflecting topographic troughs allowing additional ice flow in this area.

The next-deepest isochrone (8.7 ka, Figure 4.9) is observed at depths between 0.3H and 0.5H. The extent of this horizon is generally limited to the interior of the WAIS basin, though drawdowns appear where the surface crosses the divides toward the Thwaites Glacier and coastal Marie Byrd Land basins. Again, the observed surface does not appear affected by an inland-reaching influence of the Siple Coast ice stream flow as the simulations show. However, the Bedmap2/Shapiro experiment is again most consistent with the observed depth in this region suggesting additional integration time may make the simulated results more like the observed surface. The other simulations differ greatly, particularly in the surface depth in the interior of the Ross sector basin. The MBL+/Shapiro experiment shows a similar pattern of drawdown in the coastal Marie Byrd Land basin in an area similar to drawdown in the observed surface. Together, the simulations show this area may be a place along the divide where flow quickly diverges toward either the MBL or Siple coasts. Observed surface drawdown in the Thwaites Glacier catchment is also in an area of drawdown in the Bedmap2/Shapiro and MBL+/Shapiro experiments, but this result is not reflected in the Bedmap2/Schroeder experiment.

The 17.2 ka surface is also sometimes referred to as “Old Faithful" for its relative continuity at depth. It is believed to be the signature of a series of volcanic events at this time. This reflector is observed at depths of 0.5H to 0.75H. The MBL+/Shapiro experiment for this isochrone shows gradients in surface depth are strongly associated with the position of ice divides, which may reflect underlying issues with the vertical velocity field. Barring this possibility, it is most consistent with the relatively flat observed surface. The Bedmap2/Shapiro surface shows especially large gradients, with variations in surface depth from less than 0.1H to more to 0.9H. The Bedmap2/Schroeder surface shows a similar, though less extreme, pattern. Neither reflect the depth of the observed surface near WAIS Divide.

In an effort to map a surface older than the Last Glacial Maximum, a fourth surface is included which is observed at $\sim$0.67H and deeper (25 ka, Figure 4.11). However, the extent of this surface is limited due to the poor continuity of the observed reflector. As a result, it is hard to assess the consistency between the simulated and observed surfaces. The Bedmap2/Shapiro experiment shows a transition in depth not exhibited by the observed surface. As with the other isochrones, the two experiments using Bedmap2 topography are the most similar to each other, but the Bedmap2/Schroeder surface shows features inconsistent with ice flow suggested by shallower surfaces. This may be due to a need for more integration time and/or poor interpolation of such a deep surface with sparse isochronous contour points. The MBL+/Shapiro surface is especially poor, with no evidence of drawdown in the Thwaites Glacier catchment. This is presumably a result of poor interpolation due to particularly few contour points of this isochrone in this experiment.

4.4 Discussion

We find current model limitations affect our ability to interpret the results adequately in the context of past ice dynamics. Due to memory constraints, at most 8 evenly-spaced vertical layers are used to simulate the vertical velocity. Fewer vertical layers do not result in useful streamlines for the interpolation calculation of englacial isochronous surfaces because the path of ice flow, particularly due to shearing at depth, is not sufficiently resolved. Adjusting the distribution of the vertical layers so that there is more vertical resolution near the ice sheet bed would be prudent to better constrain particle motion in the shear zone of the ice sheet. Beyond that, increasing vertical resolution is desirable. However, this leads to increased memory usage and run times which exceed supercomputing queue limits. Use of fewer cores per node and restart capability could address these issues, but additional model development to more efficiently handle the memory requirements of increased vertical resolution are necessary to increase the vertical resolution to more than 8 layers.

There is a reasonable match between observed and modeled horizontal surface velocity, as expected by the model inversion. However, issues remain with the stability of the estimated vertical velocity. In particular, the flow transition at divides are not handled gracefully by the small number of polynomials presently in use. Unless otherwise constrained, this results in anomalous vertical velocities, including ice flow up and out of the ice sheet surface. Current and future model development is intended to address this issue, including constraining the estimated values of the vertical velocity, adding the vertical velocity to the model objective function, and increasing the weight of the vertical velocity misfit term in the objective function.

4.5 Conclusion

While model development is still needed for the model to be of most use scientifically, this analysis includes a proof of concept for deriving simulated isochronous surfaces from Ymir ice sheet model output. The results generally suggest additional iteration time is necessary. For example, the experiment with the least high-resolution boundary conditions appears to match observations best which would be the case if that experiment were converging faster than the others. Ymir-derived surfaces demonstrate greater variability in depth than the observed surfaces. This may be attributable to issues with the solution of the vertical velocity discussed previously.

Without a converged solution for each of the experiments, it would be impractical to make firm conclusions comparing simulations to each other for the purpose of sensitivity analysis or definitively suggesting one of the experiments is a better match to observations. However, the progress toward this end is promising that these objectives will be achievable with the model after further development.

4.6 Supplemental Information

4.6.1 Ymir ice sheet model version information

An instance of Ymir model version 1.1478.26c3 was used for this analysis. For the purpose of this analysis, additional patches have been made to this version, including functionality for generating VTK output in the polar stereographic projection, for the addition of thermocoupling to solve for the ice sheet temperature field, and for subglacial melting. The code and additional patches are available from the developer, Dr. Tobin Issac at the Georgia Institute of Technology School of Computational Science and Engineering.

4.6.2 Paraview scripts

The python work flow for post-processing Ymir output and Antarctic catchment information will be made available on github. Contact the author for additional information.

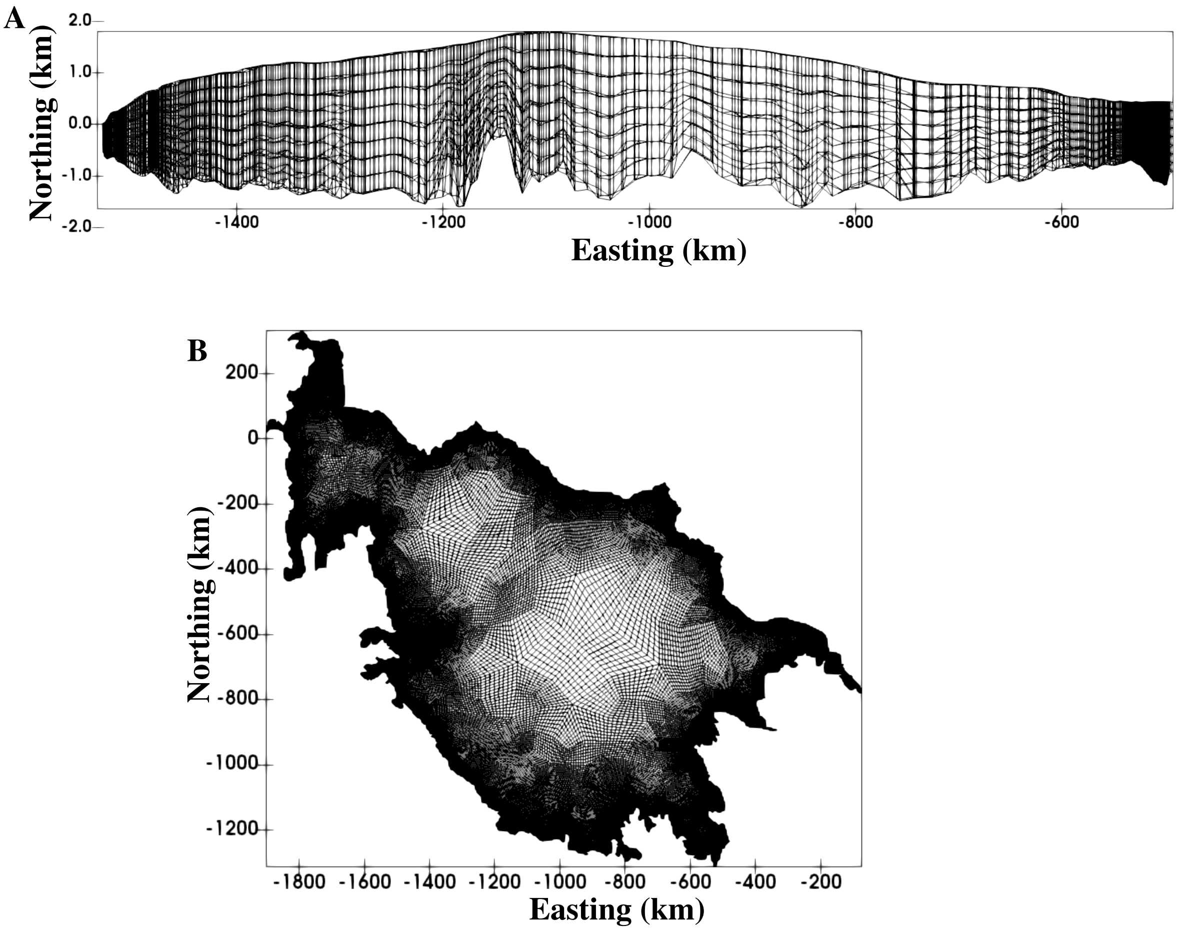

Figure 4.1: The mesh used for all model simulations has 8 vertical layers linearly distributed in depth. The horizontal mesh is refined according to the topographic geometry with a maximum horizontal-to-vertical aspect ratio of 300 in the interior. (The vertical dimension has been exaggerated 50x in this representation.)

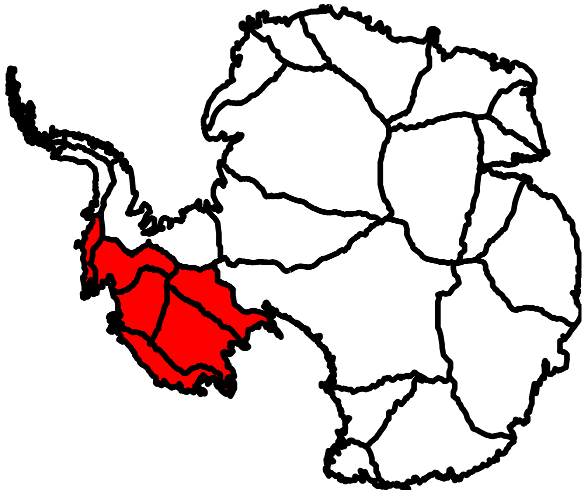

Figure 4.2: The domain used for Ymir ice sheet model experiments in this study. Antarctic Ice Sheet drainage basins are defined by Zwally et al. (2012). The domain includes basins covering most of the West Antarctic Ice Sheet, including the Belinghausen Sea Coast, Amundsen Sea Coast, Siple Coast, and WAIS Divide.

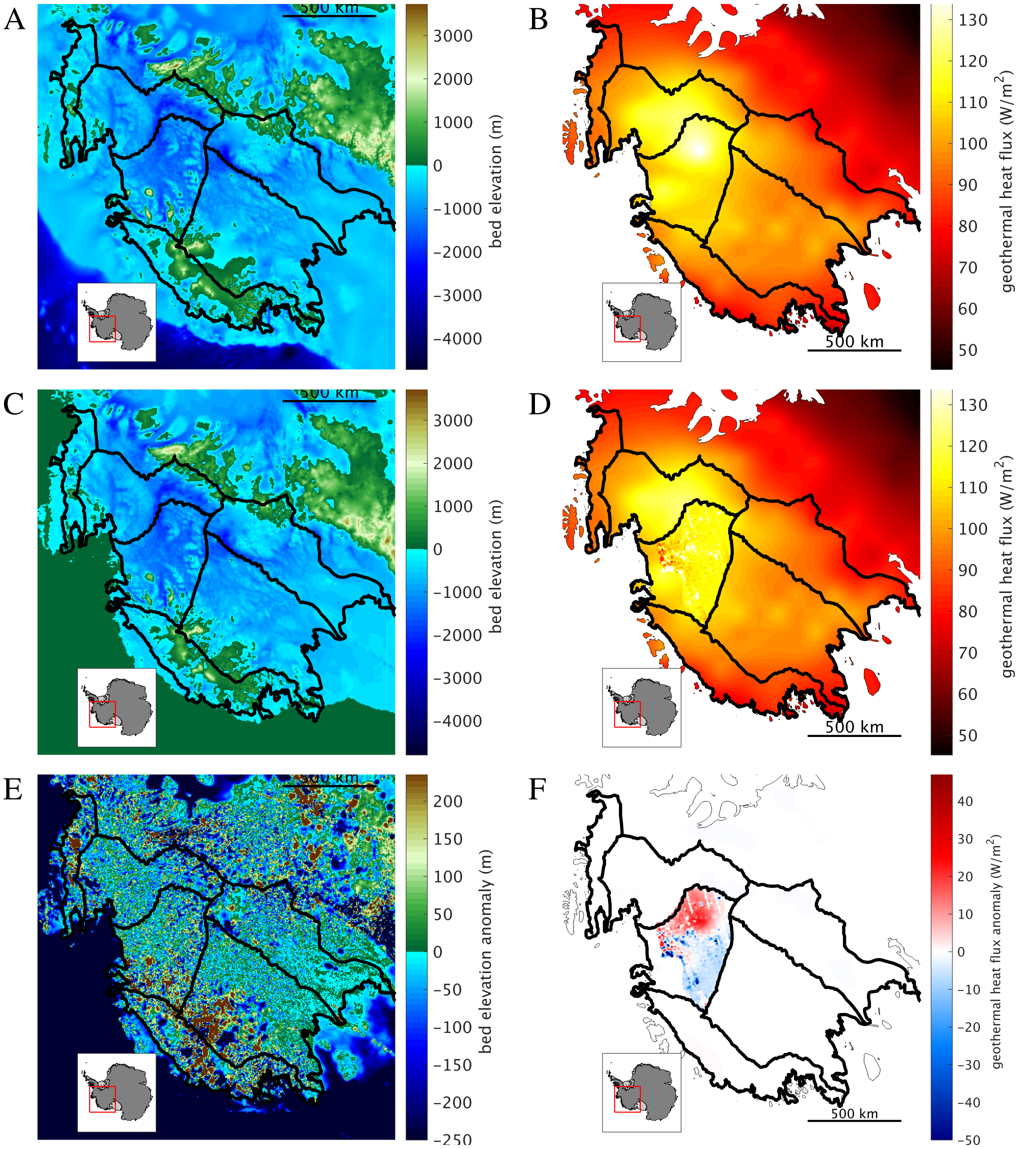

Figure 4.3: Model boundary conditions. A) Bedmap2 topography, B) Shapiro geothermal flux, C) MBL+ topography, D) Schroeder geothermal flux in Thwaites Glacier catchment with Shapiro flux elsewhere, E) anomaly between basal topographies, F) anomaly between geothermal fluxes. Positive anomalies indicate the Bedmap2 or Shapiro estimates are higher than the MBL+ and Schroeder estimates, respectively. See text for references.

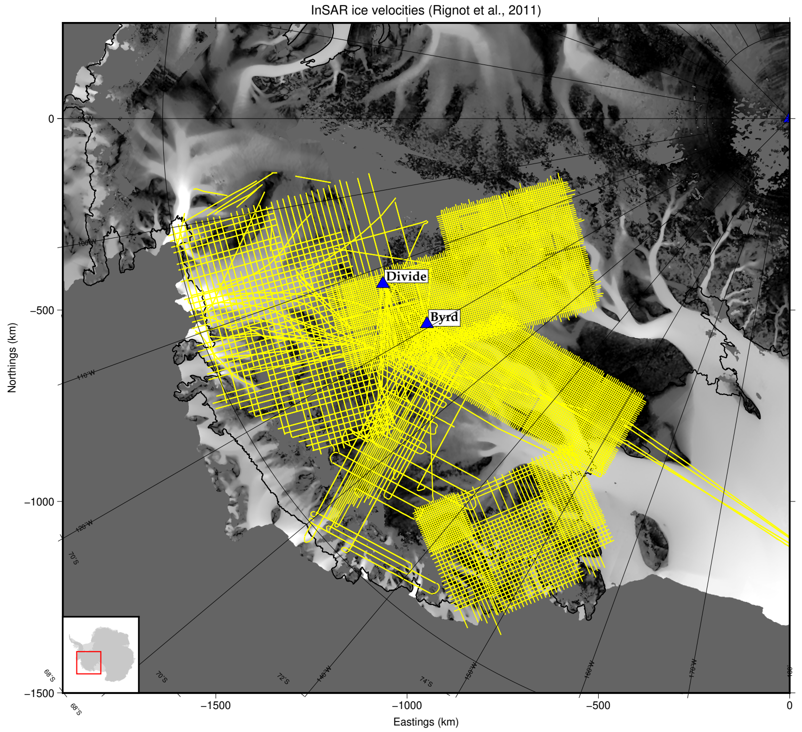

Figure 4.4: Extent of ice-penetrating radar surveys over the central West Antarctic Ice Sheet, including data from the GIMBLE (Young et al., 2012), AGASEA (Holt et al., 2006), CASERTZ (Morse et al., 2002), and SOAR/WMB (Luyendyk et al., 2003) projects.

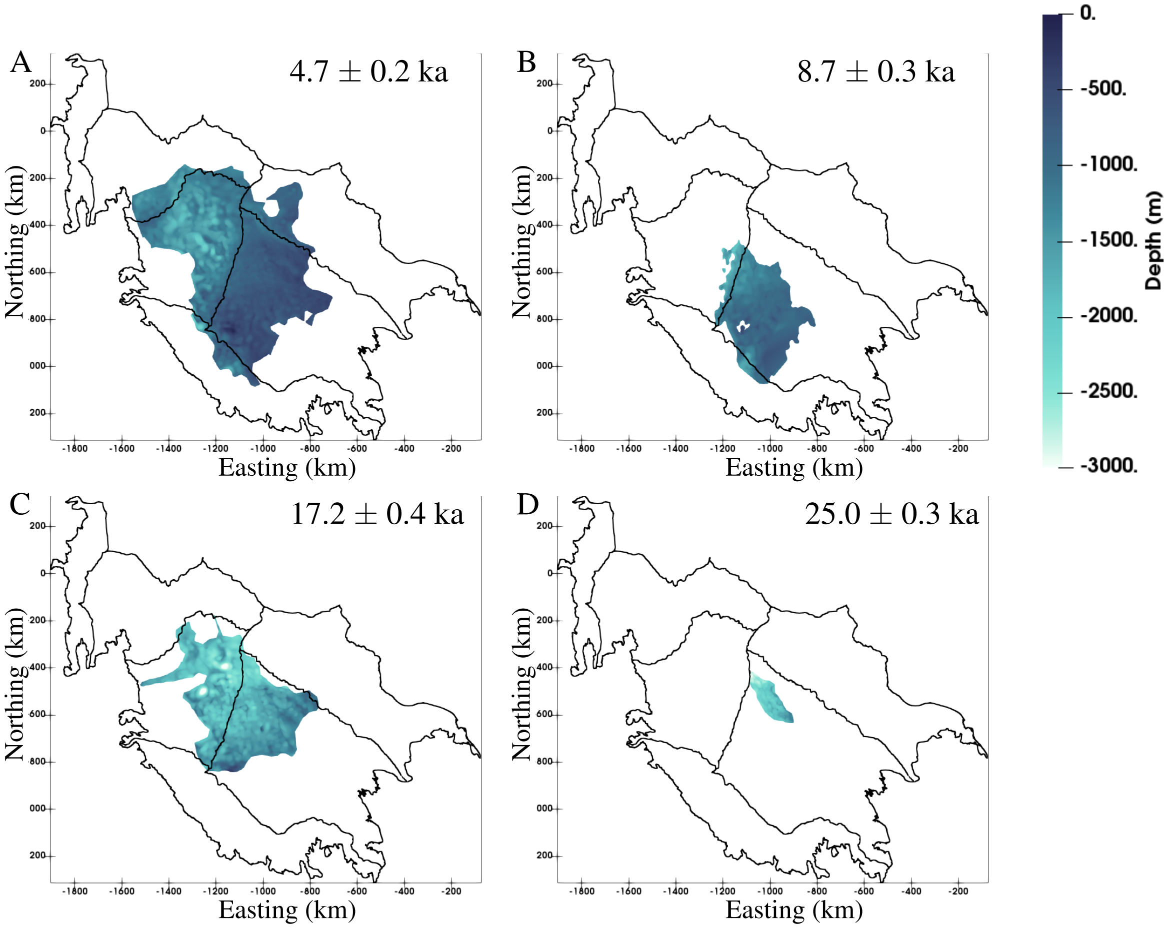

Figure 4.5: Depth to four observed isochronous englacial reflectors identified in Muldoon et al. (2018b, in review), from A) youngest (∼5ka) to D) oldest (∼25ka). The extent of each horizon is dependent on the continuity of the observed featured in analyzed radargrams. For dating purposes, all reflectors must be traced to the vicinity of at least one ice core with a published chronology, including the WAIS Divide and Byrd ice cores.

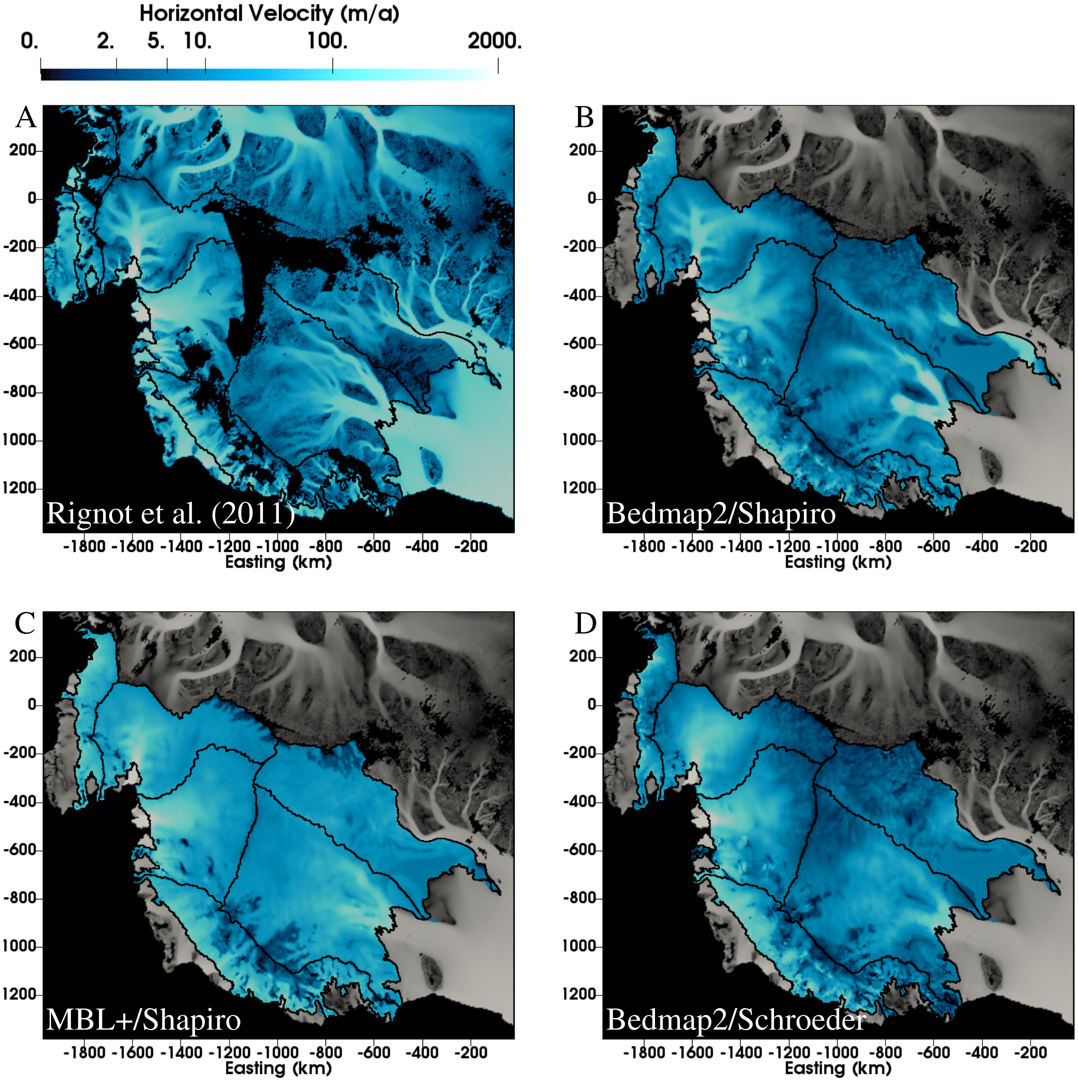

Figure 4.6: Horizontal surface velocity for A) MEaSUReS dataset (Rignot et al., 2011) used as a constraint for the model inversion, B) the Bedmap2/Shapiro experiment, C) the MBL+/Shapiro experiment, and D) the Bedmap2/Schroeder experiment. Note the velocity for the Ymir runs is only computed within the model domain, indicated by the black line. Faded velocities outside this domain in the figure are from MEaSUReS for comparison. All Ymir experiment output is shown after 6 optimization iterations.

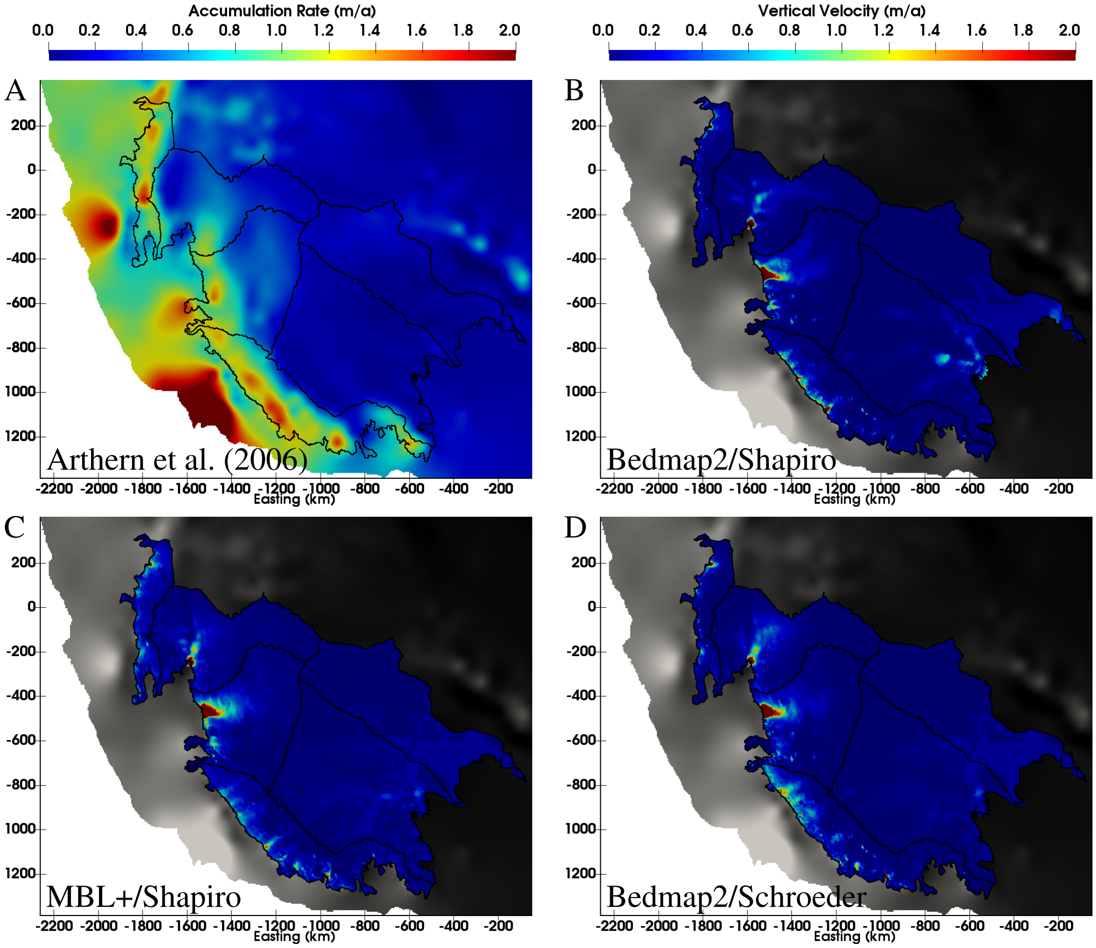

Figure 4.7: Comparison of simulated vertical ice velocity at the ice sheet surface to the surface accumulation boundary condition. A) Surface accumulation from Arthern et al. (2006) used as a model boundary condition. Surface vertical velocities from B) the Bedmap2/Shapiro experiment, C) the MBL+/Shapiro experiment, and D) the Bedmap2/Schroeder experiment. Note values of simulated vertical velocity shown are absolute values for comparison to the (positive) surface mass balance of Arthern et al. (2006). For implementation, vertical velocity is negative (down into the ice sheet).

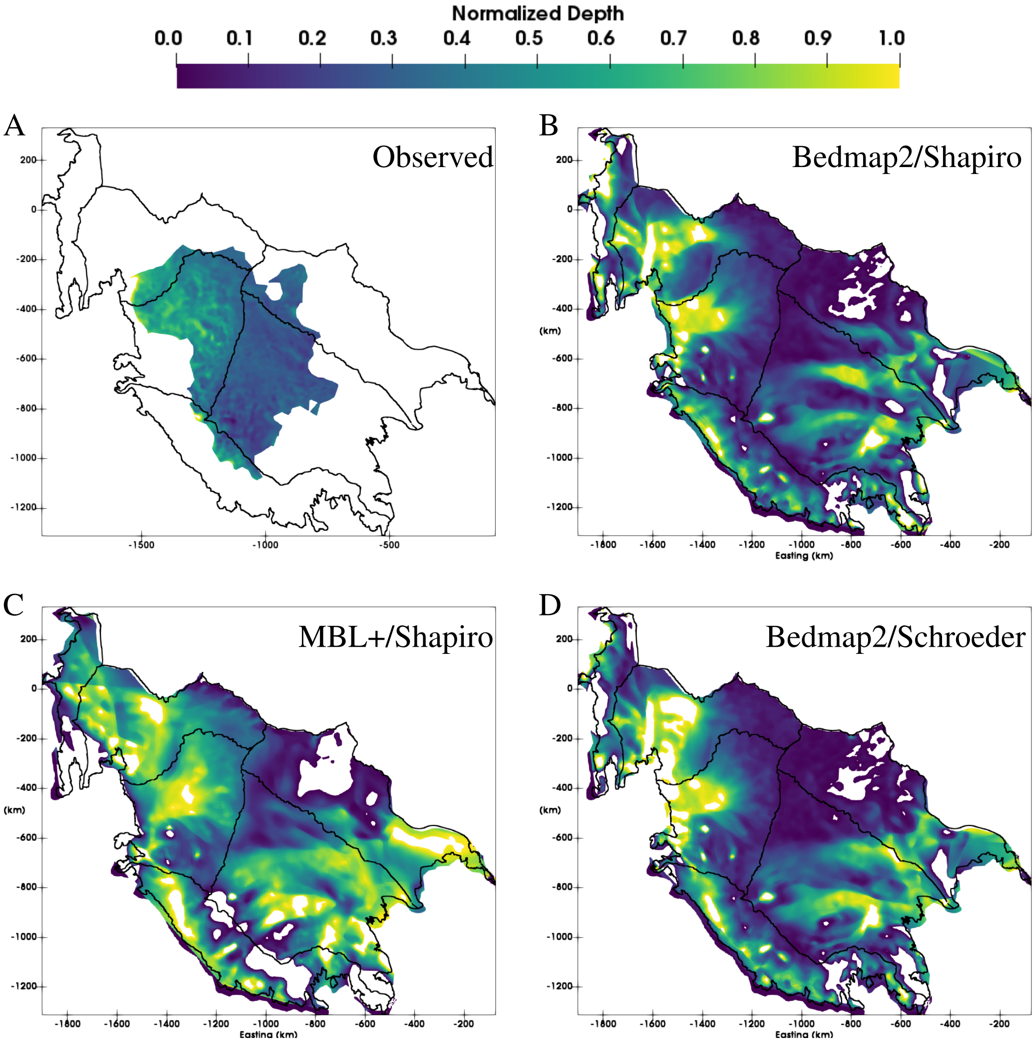

Figure 4.8: Depth to the 4.7 ka isochronous surface. A) Surface extent and depth observed using ice-penetrating radar. Simulated depths for B) the Bedmap2/Shapiro experiment, C) the MBL+/Shapiro experiment, and D) the Bedmap2/Schroeder experiment.

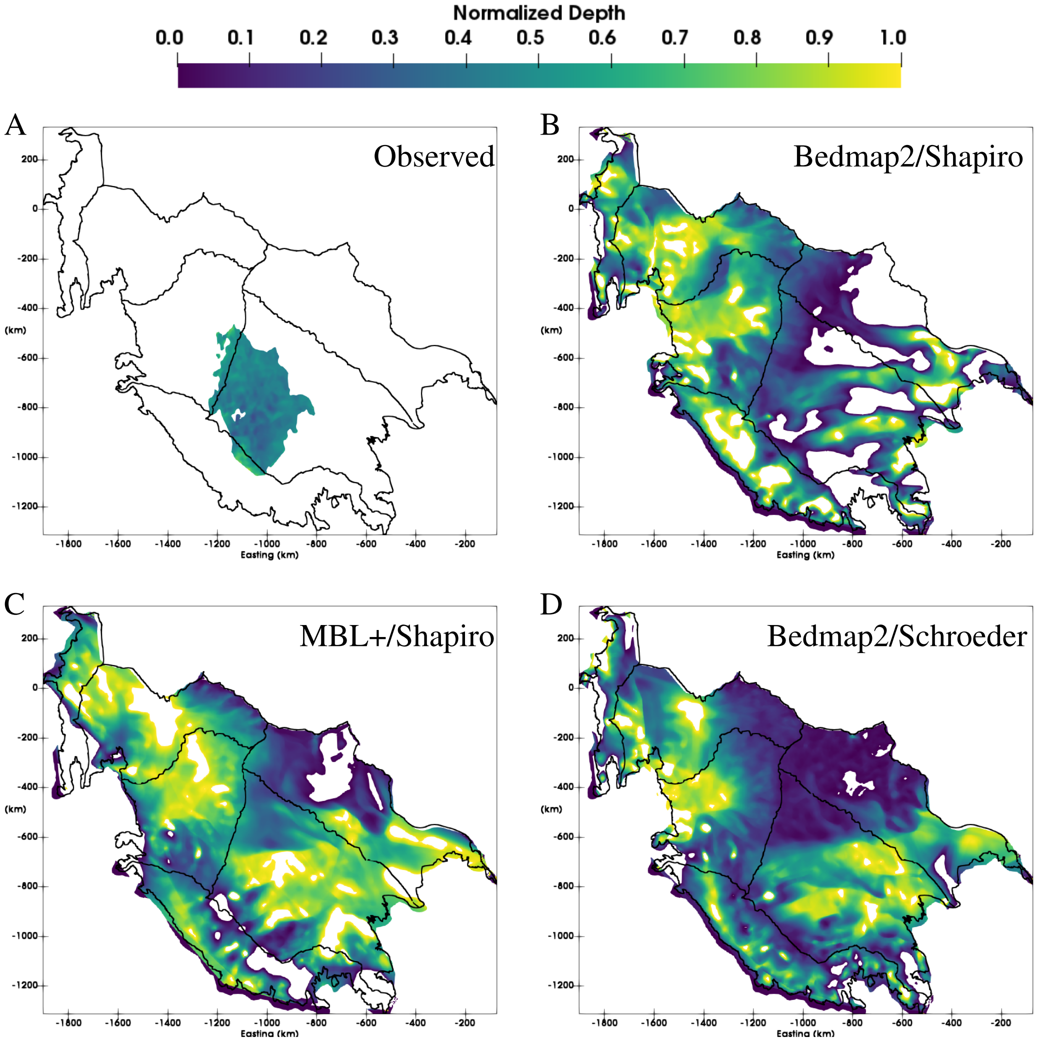

Figure 4.9: Depth to the 8.7 ka isochronous surface. A) Surface extent and depth observed using ice-penetrating radar. Simulated depths for B) the Bedmap2/Shapiro experiment, C) the MBL+/Shapiro experiment, and D) the Bedmap2/Schroeder experiment.

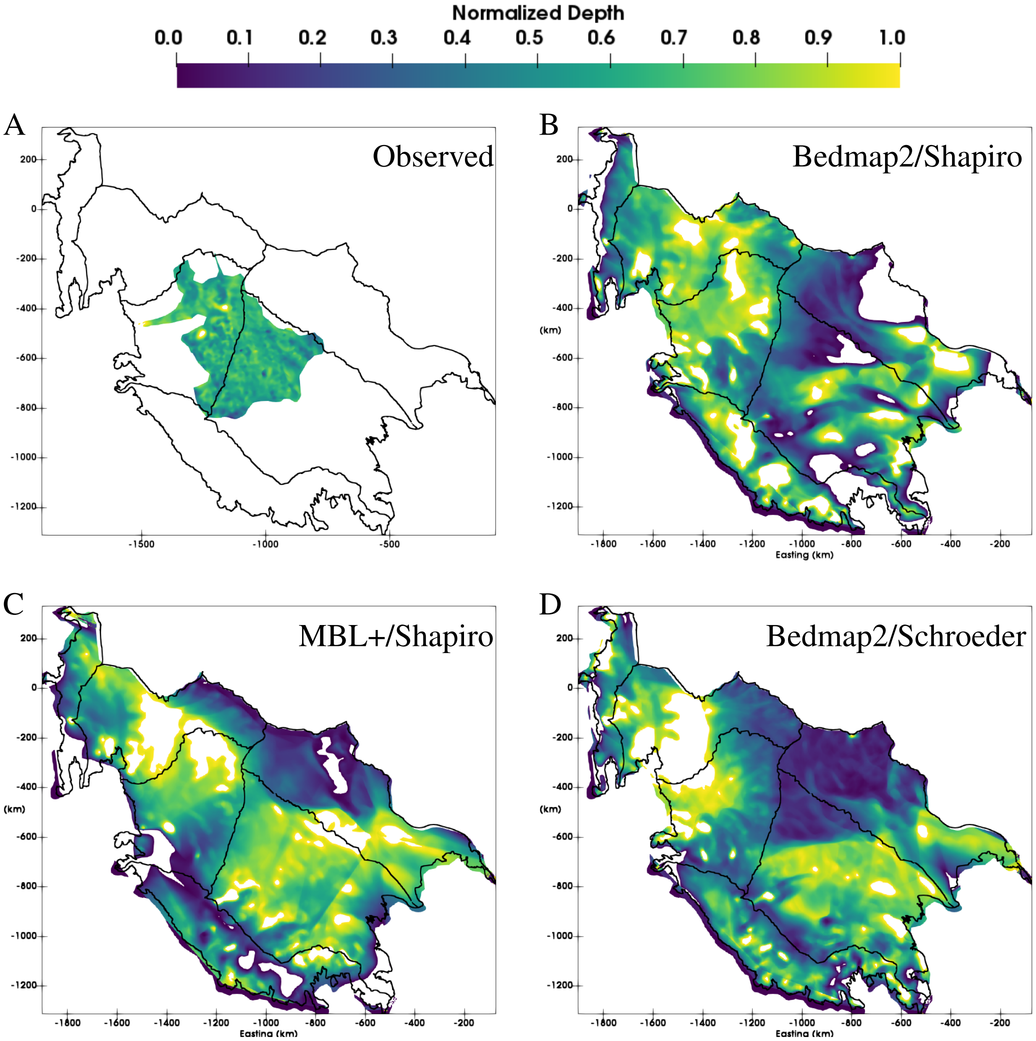

Figure 4.10: Depth to the 17.2 ka isochronous surface. A) Surface extent and depth observed using ice-penetrating radar. Simulated depths for B) the Bedmap2/Shapiro experiment, C) the MBL+/Shapiro experiment, and D) the Bedmap2/Schroeder experiment.

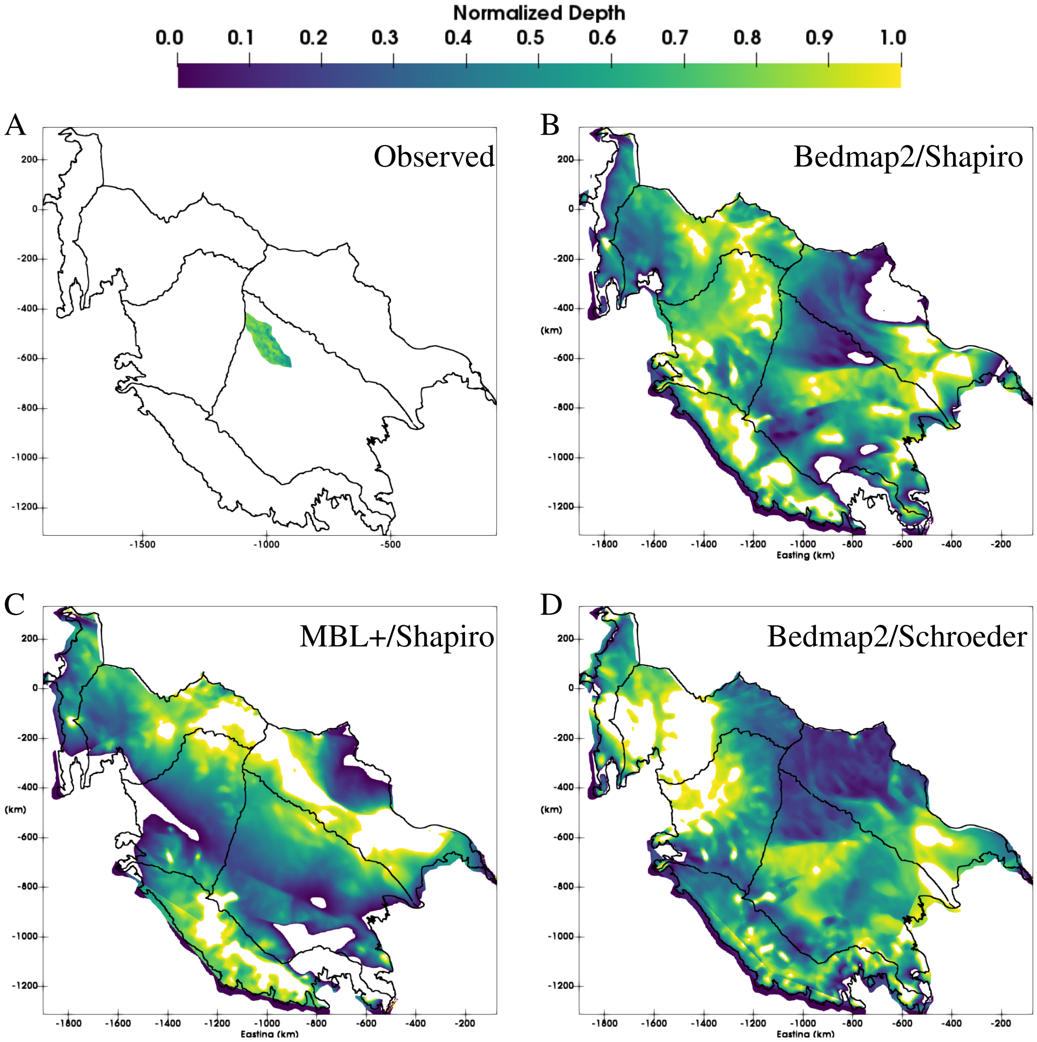

Figure 4.11: Depth to the 25 ka isochronous surface. A) Surface extent and depth observed using ice-penetrating radar. Simulated depths for B) the Bedmap2/Shapiro experiment, C) the MBL+/Shapiro experiment, and D) the Bedmap2/Schroeder experiment.

Chapter 5

Closing Remarks

5.1 Challenges

The purpose of this work has been to explore the history of the West Antarctic Ice Sheet back to the Last Interglacial. Paleoclimate data indicate higher global sea level at that time which suggests considerable ice mass loss from the Antarctic Ice Sheet. As the modern climate approaches similar temperature anomalies to the Last Interglacial (Figure 1.1), this time period can be useful as a proxy for estimating the behavior of the Antarctic Ice Sheet and its contribution to sea level in response to modern climate change.

The West Antarctic Ice Sheet is of particular importance to this problem because of its susceptibility to the hypothesized marine ice sheet instability, which suggests a positive feedback in glacial retreat of an ice sheet grounded below sea level on an upstream-sloping bed (Weertman, 1976; Schoof, 2007; Parizek et al., 2013). Modern observations of glacial thinning and ice sheet mass loss in submarine-grounded areas of the WAIS support this hypothesis (Joughin et al., 2014), as do various modeling studies which apply climate change forcing to the ice sheet (e.g. Pollard and DeConto, 2009; Bamber et al., 2009). However, uncertain boundary conditions may act to slow or stop glacial retreat, such as sub-resolution pinning points in the bed topography which can act to locally reverse the direction of the bed slope. As a result of this complexity, it is a challenge to estimate the Last Interglacial configuration of the WAIS which could guide data collection to areas with evidence of past ice sheet behavior.

This body of work includes a combination of data analysis and modeling efforts to estimate the configuration of the Antarctic Ice Sheet during the Last Interglacial. Modeling is important for estimating essential details of this complex physical system under conditions that are not well known and/or may be different from today. These conditions include poorly constrained subglacial boundary conditions as well as changes in atmospheric circulation as a result of differences of the ice sheet surface configuration. The use of two higher-order ice sheet models at various stages of this analysis demonstrates the complexity of the issue. Transient modeling (Chapter 2) is important to grasp aspects of retreat associated with changes in sea level, but there is little data to compare to the simulated results of an ice sheet which is radically different from modern ice sheets we can observe. Steady state modeling (Chapter 4) is useful for resolving the potentially complex geometry of englacial ice, observations of which do exist for comparison. However, as we expect the Antarctic Ice Sheet is not currently in steady state, these efforts are limited to the testing of end-member hypotheses about glacial retreat.

While modeling efforts can shed light on ice sheet response to external forcing, observations are necessary to act as ground truth for simulated results and constrain uncertain boundary conditions. The University of Texas has conducted several large-scale ice-penetrating radar surveys of the central WAIS, including overlap with the Byrd and WAIS Divide ice cores (Figure 4.4). Correlation between radar observations and ice core chronologies make it possible to date observed englacial horizons even at a distance from the ice core sites. This is done by tracking continuous englacial reflectors in the radar data using seismic interpretation software. In this region, several reflectors in the top two-thirds of the ice column can be traced extensively through the existing surveys. In the bottom third of the ice column, reflectors generally lack continuity and so are able to contribute only local constraints on the vertical distribution of ice as a function of time.

The oldest isochrone considered in this study is $\sim$25 ka (Chapter 3), but the extent of this surface is limited to the area between the Byrd and WAIS Divide ice cores. Because correlation to ice cores is necessary to transfer chronological information to observed radar reflectors, we consider only those englacial features that can be traced to the vicinity of an ice core. Our data analysis therefore does not rule out the presence of ice older than 25 ka, perhaps even dating to the Last Interglacial, below our deepest traceable reflectors. However, we are not able to constrain the distribution of this older ice, only the ice depth which it must be below.

Even without directly mapping Last Interglacial ice, radar observations may contain information about ice flow direction change indicative of past mass balance. To explore this, we compare observed englacial isochrones to those simulated with various boundary conditions to explore the sensitivity of isochrone geometry to uncertainty in these model constraints. While the depth and shape of englacial surfaces are impacted by ice flow, they may also deform in response to topographic boundaries or geothermal flux anomalies. Uncertainty in our knowledge of these boundary conditions therefore impacts our ability to assess the origin of model-data misfits of englacial ice surfaces and whether they can be attributed to non-steady state behavior. Though the Ymir model (Isaac et al., 2015) is still under development, we show this technique is feasible and may be more useful at higher resolution.

5.2 Primary Results

We find retreating the Antarctic Ice Sheet under Last Interglacial conditions results in mass loss consistent with the Last Interglacial sea level budget (Chapter 2; Muldoon et al., 2018a, in review; McKay et al., 2011). We also estimate the spatial distribution of ice loss and find the Marie Byrd Land highland remains intact, but the submarine basin of the central WAIS extensively retreats. This geometry is relatively insensitive to subshelf ocean forcing, but a 1 m/a subshelf melt rate is most consistent with equilibrium sea level change estimates (McKay et al., 2011).

Ice-penetrating radar surveys in the central WAIS were analyzed specifically for deep, continuous reflectors which could serve to best constrain the distribution of old[1] ice in the region which may have survived such a retreat (Chapter 3). While

---

[1] “Old" here is used relative to the West Antarctic Ice Sheet chronologies which have revealed ice as old as $\sim$135 ka (Buizert et al., 2015; Gow et al., 1968; Korotkikh et al., 2011). Significantly older—800 ka or more—ice has been observed in the thicker, more stable East Antarctic Ice Sheet (EPICA EPICA community members, 2004; Yan et al., 2017). Faster flow and higher inland-penetration of ice streams mean “old" WAIS ice is much younger than the oldest glacial ice in the EAIS.

Last Interglacial ice has been observed in blue ice areas of the WAIS (Korotkikh et al., 2011), the oldest reflector we can date between the Byrd and WAIS Divide ice cores is $\sim$25 ka, older than the Last Glacial Maximum but not approaching the Last Interglacial. This reflector occurs at about two-thirds of the ice thickness at the Byrd ice core site, constraining older ice to be in the bottom third of the ice column. Younger reflectors can also be tracked extensively through the WAIS, including the “Old Faithful" horizon which we determine to be $\sim$17 ka and located in the middle third of the ice depth. As part of this work, we compute the uncertainty on these ages from dating and radar sources and find uncertainty in the radar observations, specifically the reflector-dependent signal-to-noise, dominates uncertainty in dating englacial ice.

Chapter 4 describes progress toward using traced radar reflectors to interpolate isochronous englacial surfaces and uses simulated 3D ice velocity fields to derive their modeled counterparts. The analysis includes simulations based on different combinations of boundary conditions to test the sensitivity of englacial surface geometry on uncertain boundary conditions as opposed to ice dynamics over time. The scientific results are preliminary, as additional model development is needed to increase vertical resolution and the simulations have not had time to converge. However, we demonstrate the proof of concept of creating such surfaces and show results for an early model iteration in three experiments varying geothermal flux and basal topography.

5.3 Future Work

Two avenues of additional work would advance this research: further model development and a more sophisticated approach to mapping radar observations.

5.3.1 Model development

As discussed in Chapter 4, model efficiency including run times and memory usage have impacted our ability to obtain good estimates of the 3D velocity field from the Ymir ice sheet model (Isaac et al., 2015). Currently, a tradeoff in aspect ratio (reducing horizontal resolution to increase vertical resolution) is used to avoid memory issues prohibiting solving the problem. Additional development would help improve this situation, but functionality could also be added for restarting simulations which take longer than typical supercomputing queue limits (48 hours). Tighter integration between the temperature calculation and the optimization of ice flow equations would also be a useful advancement, though thermomechanical coupling is still a recent addition to the modeling effort.

Related to operating at higher vertical resolutions, the solution of the vertical velocity should be revisited to ensure suitable estimates particularly at ice divides. Vertical ice velocity at the ice sheet surface is now included in the model objective function, but additional development is necessary to appropriately balance the weighting of this component.

5.3.2 Data processing automation

Current methods to extract englacial surfaces from ice-penetrating radar observations are labor-intensive and rely on the brightness and continuity of reflectors in the data. As such, reflectors in areas of complex flow or topography—perhaps some of the more interesting areas for understanding ice flow history—may be truncated. These issues could be improved by a) a more automated picking algorithm and/or b) relative dating of discontinuous reflector segments in the ice column.

While human-in-the-loop methods have the advantage of identifying interesting local ice features and perhaps more intuitively navigating complicated englacial geometry, automation would allow for quicker and more extensive mapping of englacial reflections. This result could be used to paint a broader picture of the englacial ice than is realistic with semi-automated algorithms. A number of automated reflector-tracking softwares are under development to address the issue of efficiently processing the growing body of ice-penetrating reflector data (e.g. Paden, 2016; Jordan et al., 2016; de Paul Onana et al., 2015; MacGregor et al., 2015). These algorithms can map both continuous and discontinuous reflections.

Nominally, reflection surfaces must connect to an ice core to be dated and so only continuous reflections can be assigned ages. However, stratigraphy dictates relative age structure can be determined for those reflections which do not approach an ice core, allowing for the relative dating of discontinuous reflectors based on the age of reflectors above and below in the ice column (MacGregor et al., 2015). This would result in a richer dataset of englacial age information as has been performed for the Greenland Ice Sheet. Efforts to this end have been proposed and are expected in the future.

Bibliography

R. J. Arthern, D. P. Winebrenner, and D. G. Vaughan. Antarctic snow accumulation mapped using polarization of 4.3-cm wavelength microwave emission. *Journal of Geophysical Research: Atmospheres*, 111(D6), 2006.

J. L. Bamber, R. E. Riva, B. L. Vermeersen, and A. M. LeBrocq. Reassessment of the potential sea-level rise from a collapse of the West Antarctic Ice Sheet. *Science*, 324(5929):901–903, 2009.

N. L. Bindoff, J. Willebrand, V. Artale, A. Cazenave, J. M. Gregory, S. Gulev, K. Hanawa, C. Le Quéré, S. Levitus, Y. Nojiri, et al. Observations: oceanic climate change and sea level. 2007.

R. Bintanja and R. Van de Wal. North American ice-sheet dynamics and the onset of 100,000-year glacial cycles. *Nature*, 454(7206):869–872, 2008.

D. D. Blankenship, R. E. Bell, S. M. Hodge, J. M. Brozena, J. C. Behrendt, and C. A. Finn. Active volcanism beneath the West Antarctic ice sheet and implications for ice-sheet stability. *Nature*, 361(6412):526–529, 1993.

T. Blunier and E. J. Brook. Timing of Millennial-Scale Climate Change in Antarctica and Greenland During the Last Glacial Period. *Science*, 291(5501):109–112, 2001. doi: 10.1126/science.291.5501.109. URL `http://www.sciencemag.org/content/291/5501/109.abstract`.

C. Buizert, K. Cuffey, J. Severinghaus, D. Baggenstos, T. Fudge, E. Steig, B. Markle, M. Winstrup, R. Rhodes, E. Brook, et al. The WAIS Divide deep ice core WD2014 chronology–Part 1: Methane synchronization (68–31 ka BP) and the gas age–ice age difference. *Climate of the Past*, 11(2):153–173, 2015.

M. G. Cavitte, D. D. Blankenship, J. V. Johnson, D. A. Young, S. P. Carter, G. Gutowski, M. J. Siegert, and C. S. Jackson. Constraints on transient fast flow at South Pole in the last glacial cycle. *AGU Fall Meeting Abstracts*, page A514, Dec. 2013b.

M. G. Cavitte, D. D. Blankenship, D. A. Young, D. M. Schroeder, F. Parrenin, E. Lemeur, J. A. Macgregor, and M. J. Siegert. Deep radiostratigraphy of the East Antarctic plateau: connecting the Dome C and Vostok ice core sites. *Journal of Glaciology*, 62(232):323–334, 2016.

S. L. Cornford, D. F. Martin, D. T. Graves, D. F. Ranken, A. M. Le Brocq, R. M. Gladstone, A. J. Payne, E. G. Ng, and W. H. Lipscomb. Adaptive mesh, finite volume modeling of marine ice sheets. *Journal of Computational Physics*, 232 (1):529–549, Jan. 2013.

S. L. Cornford, D. F. Martin, V. Lee, A. J. Payne, and E. G. Ng. Adaptive mesh refinement versus subgrid friction interpolation in simulations of Antarctic ice dynamics. *Annals of Glaciology*, 57(73), 2016. doi: 10.1017/aog.2016.13.

K. M. Cuffey and W. S. B. Paterson. *The Physics of Glaciers*. Academic Press, 2010.

R. A. Dalrymple, L. Breaker, B. Brooks, D. Cayan, G. Griggs, W. Han, B. Horton, C. Hulbe, J. McWilliams, P. Mote, et al. Sea-Level Rise for the Coasts of California, Oregon, and Washington: Past, Present, and Future. *National Research, Council The National Academies Press, Washington DC*, 2012.

W. Dansgaard and S. J. Johnsen. A flow model and a time scale for the ice core from Camp Century, Greenland. *Journal of Glaciology*, 8:215–223, June 1969.

V. de Paul Onana, L. S. Koenig, J. Ruth, M. Studinger, and J. P. Harbeck. A semi-automated multilayer picking algorithm for ice-sheet radar echograms applied to ground-based near-surface data. *IEEE Transactions on Geoscience and Remote Sensing*, 53(1):51–69, 2015.

R. M. DeConto and D. Pollard. Contribution of Antarctica to past and future sea-level rise. *Nature*, 531(7596):591, 2016.

C. Deser, A. Capotondi, R. Saravanan, and A. S. Phillips. Tropical pacific and atlantic climate variability in ccsm3. *Journal of Climate*, 19(11):2451–2481, 2006.

J. A. Dowdeswell and S. Evans. Investigations of the form and flow of ice sheets and glaciers using radio-echo sounding. *Reports on Progress in Physics*, 67(10): 1821, 2004.

EPICA EPICA community members. Eight glacial cycles from an Antarctic ice core. *Nature*, 429:623–628, 2004.

C. J. Fogwill, C. S. Turney, K. J. Meissner, N. R. Golledge, P. Spence, J. L. Roberts, M. H. England, R. T. Jones, and L. Carter. Testing the sensitivity of the East Antarctic Ice Sheet to Southern Ocean dynamics: past changes and future implications. *Journal of Quaternary Science*, 29(1):91–98, 2014.

P. Fretwell, H. Pritchard, D. Vaughan, J. Bamber, N. Barrand, R. Bell, C. Bianchi, R. Bingham, D. Blankenship, G. Casassa, et al. Bedmap2: improved ice bed, surface and thickness datasets for Antarctica. *The Cryosphere Discussions*, 6: 4305–4361, 2012.

S. Fujita, H. Maeno, S. Uratsuka, T. Furukawa, S. Mae, Y. Fujii, and O. Watanabe. Nature of radio echo layering in the Antarctic ice sheet detected by a two-frequency experiment. *Journal of Geophysical Research: Solid Earth*, 104(B6): 13013–13024, 1999.

S. Fujita, T. Matsuoka, T. Ishida, K. Matsuoka, and S. Mae. A summary of the complex dielectric permittivity of ice in the megahertz range and its applications for radar sounding of polar ice sheets. *Physics of Ice Core Records*, pages 185–212, 2000.

A. E. Gelfand, A. F. Smith, and T.-M. Lee. Bayesian analysis of constrained parameter and truncated data problems using Gibbs sampling. *Journal of the American Statistical Association*, 87(418):523–532, 1992.

J. A. Goff, E. M. Powell, D. A. Young, and D. D. Blankenship. Instruments and Methods Conditional simulation of Thwaites Glacier (Antarctica) bed topography for flow models: incorporating inhomogeneous statistics and channelized morphology. *Journal of Glaciology*, 60(222):635, 2014.

A. J. Gow. Preliminary results of studies of ice cores from the 2164 m deep drill hole, Byrd Station, Antarctica. *IAHS Publ*, 86:78–90, 1970.

A. J. Gow, H. T. Ueda, and D. E. Garfield. Antarctic Ice Sheet: Preliminary Results of First Core Hole to Bedrock. *Science*, 161:1011–1013, Sept. 1968. doi: 10.1126/science.161.3845.1011.

C. Hammer, H. Clausen, and C. Langway. 50,000 years of recorded global volcanism. *Climatic Change*, 35(1):1–15, 1997.

W. K. Hastings. Monte Carlo sampling methods using Markov chains and their applications. *Biometrika*, 57(1):97–109, 1970.

P. R. Holland, A. Jenkins, and D. M. Holland. The response of ice shelf basal melting to variations in ocean temperature. *Journal of Climate*, 21(11):2558–2572, 2008.

P. R. Holland, A. Jenkins, and D. M. Holland. Ice and ocean processes in the Bellingshausen Sea, Antarctica. *Journal of Geophysical Research: Oceans*, 115 (C5), 2010.

N. Holschuh, D. Pollard, R. Alley, and S. Anandakrishnan. Evaluating Marie Byrd Land stability using an improved basal topography. *Earth and Planetary Science Letters*, 408:362–369, 2014.

J. W. Holt, D. D. Blankenship, D. L. Morse, D. A. Young, M. E. Peters, S. D. Kempf, T. G. Richter, D. G. Vaughan, and H. F. J. Corr. New boundary conditions for the West Antarctic Ice Sheet: Subglacial topography of the Thwaites and Smith glacier catchments. *Geophysical Research Letters*, 33:L09502, May 2006. doi: 10.1029/2005GL025561.

J. W. Hurrell, M. M. Holland, P. R. Gent, S. Ghan, J. Kay, and Coauthors. The Community Earth System Model: A Framework for Collaborative Research. *Bulletin of the American Meteorological Society*, 94(9):1339–1360, Feb 2013. ISSN 0003-0007.

T. Isaac, N. Petra, G. Stadler, and O. Ghattas. Scalable and efficient algorithms for the propagation of uncertainty from data through inference to prediction for large-scale problems, with application to flow of the Antarctic ice sheet. *Journal of Computational Physics*, 296:348–368, 2015.

T. Jordan, J. Bamber, C. Williams, J. Paden, M. Siegert, P. Huybrechts, O. Gagliardini, and F. Gillet-Chaulet. An ice-sheet-wide framework for englacial attenuation from ice-penetrating radar data. *The Cryosphere*, 10(4):1547, 2016.

I. Joughin and R. B. Alley. Stability of the West Antarctic ice sheet in a warming world. *Nature Geoscience*, 4:506–513, Aug. 2011. doi: 10.1038/ngeo1194.

I. Joughin, B. E. Smith, and B. Medley. Marine Ice Sheet Collapse Potentially Under Way for the Thwaites Glacier Basin, West Antarctica. *Science*, 344(6185): 735–738, 2014.

R. E. Kopp, F. J. Simons, J. X. Mitrovica, A. C. Maloof, and M. Oppenheimer. Probabilistic assessment of sea level during the last interglacial stage. *Nature*, 462(7275):863–867, 2009.

E. V. Korotkikh, P. A. Mayewski, M. J. Handley, S. B. Sneed, D. S. Introne, A. V. Kurbatov, N. W. Dunbar, and W. C. McIntosh. The last interglacial as represented in the glaciochemical record from Mount Moulton Blue Ice Area, West Antarctica. *Quaternary Science Reviews*, 30(15-16):1940–1947, 2011.

E. Larour, H. Seroussi, M. Morlighem, and E. Rignot. Continental scale, high order, high spatial resolution, ice sheet modeling using the Ice Sheet System Model (ISSM). *Journal of Geophysical Research: Earth Surface*, 117(F1), 2012.

G. Leysinger Vieli, R. Hindmarsh, and M. Siegert. Three-dimensional flow influences on radar layer stratigraphy. *Annals of Glaciology*, 46(1):22–28, 2007.

B. P. Luyendyk, D. S. Wilson, and C. S. Siddoway. Eastern margin of the Ross Sea Rift in western Marie Byrd Land, Antarctica: Crustal structure and tectonic devleopment. *Geochemistry Geophysics Geosystems*, 4, 2003. doi: 10.1029/2002GC000462.

J. A. MacGregor, G. A. Catania, H. Conway, D. M. Schroeder, I. Joughin, D. A. Young, S. D. Kempf, and D. D. Blankenship. Weak bed control of the eastern shear margin of Thwaites Glacier, West Antarctica. *Journal of Glaciology*, 59 (217):900–912, 2013.

J. A. MacGregor, M. A. Fahnestock, G. A. Catania, J. D. Paden, S. Prasad Gogineni, S. K. Young, S. C. Rybarski, A. N. Mabrey, B. M. Wagman, and M. Morlighem. Radiostratigraphy and age structure of the Greenland Ice Sheet. *Journal of Geophysical Research: Earth Surface*, 120(2):212–241, 2015.

Y. M. Martos, M. Catalán, T. A. Jordan, A. Golynsky, D. Golynsky, G. Eagles, and D. G. Vaughan. Heat flux distribution of Antarctica unveiled. *Geophysical Research Letters*, 44(22), 2017.

C. F. Maule, M. E. Purucker, N. Olsen, and K. Mosegaard. Heat flux anomalies in Antarctica revealed by satellite magnetic data. *Science*, 309(5733):464–467, 2005.

N. P. McKay, J. T. Overpeck, and B. L. Otto-Bliesner. The role of ocean thermal expansion in Last Interglacial sea level rise. *Geophysical Research Letters*, 38 (14), 2011.

D. Millar. Acidity levels in ice sheets from radio echo-sounding. *Ann. Glaciol*, 3: 199–203, 1982.

M. Morlighem, H. Seroussi, E. Larour, and E. Rignot. Inversion of basal friction in Antarctica using exact and incomplete adjoints of a higher-order model. *Journal of Geophysical Research: Earth Surface*, 118(3):1746–1753, 2013.

D. L. Morse, D. D. Blankenship, E. D. Waddington, and T. A. Neumann. A site for deep ice coring in West Antarctica: results from aerogeophysical surveys and thermo-kinematic modeling. *Annals of Glaciology*, 35(1):36–44, 2002.

G. R. Muldoon, C. S. Jackson, D. F. Martin, D. A. Young, M. S. Waibel, and D. D. Blankenship. Configuration and sea level contribution from the Antarctic Ice Sheet during the Last Interglacial. *Journal of Climate*, 2018a, in review.

G. R. Muldoon, C. S. Jackson, D. A. Young, and D. D. Blankenship. Bayesian estimation of englacial radar chronology in Central West Antarctica. *Dynamics and Statistics of the Climate System*, 2018b, in review.

M. J. O'Leary, P. J. Hearty, W. G. Thompson, M. E. Raymo, J. X. Mitrovica, and J. M. Webster. Ice sheet collapse following a prolonged period of stable sea level during the last interglacial. *Nature Geoscience*, 6(9):796–800, 2013.

J. D. Paden. Advances in Ice Penetrating Radar. *AGU Fall Meeting Abstracts*, art. C23C-01, Dec. 2016.

B. Parizek, K. Christianson, S. Anandakrishnan, R. Alley, R. Walker, R. Edwards, D. Wolfe, G. Bertini, S. Rinehart, R. Bindschadler, et al. Dynamic (in) stability of Thwaites Glacier, West Antarctica. *Journal of Geophysical Research: Earth Surface*, 118(2):638–655, 2013.

F. Parrenin, M. G. Cavitte, D. D. Blankenship, J. Chappellaz, H. Fischer, O. Gagliardini, V. Masson-Delmotte, O. Passalacqua, C. Ritz, J. Roberts, et al. Is there 1.5 million-year old ice near Dome C, Antarctica. *The Cryosphere Discuss., https://doi. org/10.5194/tc-2017-69, in review*, 2017.

M. E. Peters, D. D. Blankenship, S. P. Carter, S. D. Kempf, D. A. Young, and J. W. Holt. Along-track focusing of airborne radar sounding data from West Antarctica for improving basal reflection analysis and layer detection. *Geoscience and Remote Sensing, IEEE Transactions on*, 45(9):2725–2736, 2007.

N. Petra, H. Zhu, G. Stadler, T. J. Hughes, and O. Ghattas. An inexact Gauss–Newton method for inversion of basal sliding and rheology parameters in a nonlinear Stokes ice sheet model. *Journal of Glaciology*, 58(211):889–903, 2012.

D. Pollard and R. M. DeConto. Modelling West Antarctic ice sheet growth and collapse through the past five million years. *Nature*, 458(7236):329–332, Mar. 2009.

D. Pollard, R. M. DeConto, and R. B. Alley. Potential Antarctic Ice Sheet retreat driven by hydrofracturing and ice cliff failure. *Earth and Planetary Science Letters*, 412:112–121, 2015.

H. Pritchard, S. Ligtenberg, H. Fricker, D. Vaughan, M. Van den Broeke, and L. Padman. Antarctic ice-sheet loss driven by basal melting of ice shelves. *Nature*, 484(7395):502–505, 2012.

A. Quiquet, C. Ritz, H. Punge, and D. Salas y Mélia. Greenland ice sheet contribution to sea level rise during the last interglacial period: a modelling study driven and constrained by ice core data. *Climate of the Past*, 9(1):353–366, 2013.

E. Rignot, J. Mouginot, and B. Scheuchl. Ice flow of the Antarctic ice sheet. *Science*, 333(6048):1427–1430, 2011.

G. d. Q. Robin, S. Evans, and J. T. Bailey. Interpretation of radio echo sounding in polar ice sheets. *Philosophical Transactions of the Royal Society of London A: Mathematical, Physical and Engineering Sciences*, 265(1166):437–505, 1969.

R. P. Scherer, A. Aldahan, S. Tulaczyk, G. Possnert, H. Engelhardt, and B. Kamb. Pleistocene collapse of the West Antarctic ice sheet. *Science*, 281(5373):82–85, 1998.

C. Schoof. Ice sheet grounding line dynamics: Steady states, stability, and hysteresis. *Journal of Geophysical Research: Earth Surface*, 112(F3), 2007.

D. M. Schroeder, D. D. Blankenship, D. A. Young, and E. Quartini. Evidence for elevated and spatially variable geothermal flux beneath the West Antarctic Ice Sheet. *Proceedings of the National Academy of Sciences*, 111(25):9070–9072, 2014.

J. Schwander, J. Jouzel, C. U. Hammer, J.-R. Petit, R. Udisti, and E. Wolff. A tentative chronology for the EPICA Dome Concordia ice core. *Geophysical Research Letters*, 28:4243–4246, Nov. 2001. doi: 10.1029/2000GL011981.

N. M. Shapiro and M. H. Ritzwoller. Inferring surface heat flux distributions guided by a global seismic model: particular application to Antarctica. *Earth and Planetary Science Letters*, 223(1):213–224, 2004.

M. J. Siegert, R. Hodgkinst, and J. A. Dowdeswell. Internal radio-echo layering at Vostok station, Antarctica, as an independent stratigraphic control on the ice-core record. *Annals of Glaciology*, 27(1):360–364, 1998.

M. J. Siegert, B. Welch, D. Morse, A. Vieli, D. D. Blankenship, I. Joughin, E. C. King, J.-M. Gwendolyn, A. J. Payne, and R. Jacobel. Ice flow direction change in interior West Antarctica. *Science*, 305(5692):1948–1951, 2004.

E. Stone, D. Lunt, J. Annan, and J. Hargreaves. Quantification of the Greenland ice sheet contribution to Last Interglacial sea level rise. *Climate of the Past*, 9(2): 621–639, 2013.

J. O. Stone, G. A. Balco, D. E. Sugden, M. W. Caffee, L. C. Sass, S. G. Cowdery, and C. Siddoway. Holocene deglaciation of Marie Byrd land, west Antarctica. *Science*, 299(5603):99–102, 2003.

T. Thorsteinsson and E. D. Waddington. Folding in strongly anisotropic layers near ice-sheet centers. *Annals of Glaciology*, 35(1):480–486, 2002.

J. Turner, A. Orr, G. H. Gudmundsson, A. Jenkins, R. G. Bingham, C.-D. Hillenbrand, and T. J. Bracegirdle. Atmosphere-ocean-ice interactions in the Amundsen Sea Embayment, West Antarctica. *Reviews of Geophysics*, 55(1):235–276, 2017.

D. G. Vaughan, P. S. Anderson, J. C. King, G. W. Mann, S. D. Mobbs, and R. S. Ladkin. Imaging of firn isochrones across an Antarctic ice rise and implications for patterns of snow accumulation rate. *Journal of Glaciology*, 50:413–418, 2004. doi: 10.3189/172756504781829882.

E. D. Waddington, J. F. Bolzan, and R. B. Alley. Potential for stratigraphic folding near ice-sheet centers. *Journal of Glaciology*, 47(159):639–648, 2001.

J. Weertman. Sliding-no sliding zone effect and age determination of ice cores. *Quaternary Research*, 6(2):203–207, 1976.

D. Wiens, W. Shen, S. Anandakrishnan, R. Aster, P. Gerstoft, P. Bromirski, I. Dalziel, S. Hansen, D. Heeszel, A. Huerta, et al. Seismic and thermal structure of the crust and uppermost mantle beneath Antarctica from inversion of multiple seismic datasets. In *AGU Fall Meeting Abstracts*, 2017.

R. Winkelmann, M. A. Martin, M. Haseloff, T. Albrecht, E. Bueler, C. Khroulev, and A. Levermann. The Potsdam Parallel Ice Sheet Model (PISM-PIK) Part 1: Model description. *The Cryosphere*, 5:715–726, 2011. doi: 10.5194/tc-5-715-2011.

M. Winsborrow, C. D. Clark, and C. R. Stokes. What controls the location of ice streams? *Earth-Science Reviews*, 103(1):45–59, 2010.

U. N. E. P. World Glacier Monitoring Service. Global glacier changes: facts and figures. *Geneva: uNEP/WGMS*, 2008.

Y. Yan, J. Ng, J. A. Higgins, A. Kurbatov, H. Clifford, N. Spaulding, J. Severinghaus, E. Brook, P. Mayewski, and M. Bender. 2.7-Million-Year-Old Ice from Allan Hills Blue Ice Areas, East Antarctica Reveals Climate Snapshots Since Early Pleistocene. In *Goldschmidt Conference, 2017. Proceedings. European Association of Geochemistry and Geochamical Society*, 2017.

D. A. Young, A. P. Wright, J. L. Roberts, R. C. Warner, N. W. Young, J. S. Greenbaum, D. M. Schroeder, J. W. Holt, D. E. Sugden, D. D. Blankenship, et al. A dynamic early East Antarctic Ice Sheet suggested by ice-covered fjord landscapes. *Nature*, 474(7349):72–75, 2011.

D. A. Young, D. D. Blankenship, and J. W. Holt. GIMBLE: Geophysical Investigations of Marie Byrd Land Evolution: a new airborne survey of the linchpin of the West Antarctic. *WAIS Workshop 2012*, 2012.

D. A. Young, D. Schroeder, D. Blankenship, S. D. Kempf, and E. Quartini. The distribution of basal water between Antarctic subglacial lakes from radar sounding. *Phil. Trans. R. Soc. A*, 374(2059):20140297, 2016.

D. A. Young, D. D. Blankenship, S. D. Kempf, E. Quartini, G. R. Muldoon, and E. M. Powell. Ice thickness and related data over central Marie Byrd Land, West Antarctica Antarctica (GIMBLE.GR2HI2). Technical report, UTIG, 2017.

H. Zhu, N. Petra, G. Stadler, T. Isaac, T. J. Hughes, and O. Ghattas. Inversion of geothermal heat flux in a thermomechanically coupled nonlinear Stokes ice sheet model. *The Cryosphere*, 10(4):1477–1494, 2016.

H. J. Zwally, M. B. Giovinetto, M. A. Beckley, and J. L. Saba. Antarctic and Greenland drainage systems. *GSFC Cryospheric Sciences Laboratory*, 2012.

Vita

Gail Muldoon grew up in Lusby, Maryland. In 2010, she graduated from Haverford College with a B.S. in Astronomy and Physics. Her undergraduate thesis involved observational optical astronomy research. She then moved to Austin, Texas and joined the staff of the University of Texas Institute for Geophysics as a Research Scientist Assistant doing coupled earth system modeling focused on ice sheet behavior. She entered the graduate school at the University of Texas in 2011 and obtained an M.S. in 2013 for work modeling surface mass balance biases over the Greenland Ice Sheet. Following her M.S., she switched focus to Antarctic Ice Sheet behavior during the Last Interglacial. She participated in two field seasons in West Antarctica in 2012-2013 and 2014-2015. While at UT, Gail worked as a research assistant and teaching assistant for courses in geology and climate science. Starting in 2015, she supervised summer interns interpreting ice-penetrating radar observations. In 2015, she completed a Portfolio in Applied Statistical Modeling at the University of Texas. During her graduate career, Gail presented at dozens of conferences around the world and received the Fred M. Bullard Student Research Fellowship, the Muehlberger Field Scholarship, and the Department of Geological Sciences Outstanding Teaching Assistant Award.

Permanent address: 1201 Enterprise Avenue, Apartment 803
League City, Texas 77573

This dissertation was typeset with LaTeX[†] by the author.

[†] LaTeX is a document preparation system developed by Leslie Lamport as a special version of Donald Knuth's TeX Program.